1
2
3
4
5
6
7
8
9
10
11
12
13
14
15
16
17
18
19
20
21
22
23
24
25
26
27
28
29
30
31
32
33
34
35
36
37
38
39
40
41
42
43
44
45
46
47
48
49
50
51
52
53
54
55
56
57
58
59
60
61
62
63
64
65

Composition engineering of ZIF-derived cobalt phosphide/cobalt monoxide heterostructures for high-performance asymmetric supercapacitors

Sampath Gayathri,[1] Paulraj Arunkumar,[1] Dipankar Saha,[2] and Jong Hun Han[1,*]

[1]*School of Chemical Engineering, Chonnam National University, 300 Yongbong-dong, Buk-gu, Gwangju 61186, Republic of Korea. Email: jhhan@chonnam.ac.kr*
[2]*Center for Materials Science and Nanotechnology, Department of Chemistry, University of Oslo, P.O. Box 1033, Blindern, N-0315 Oslo, Norway.*

1

Abstract

The fabrication of interpenetrated heterostructures from desirable energy materials for the development of efficient supercapacitor devices is promising yet challenging. Herein, a leaf-shaped cobalt phosphide/cobalt oxide heterostructure, $(CoP_x)_{1-y}/CoO_y$ ($0.44 > y > 0.06$), was synthesized from a 2D-zeolitic-imidazolate-framework (ZIF-Co-L) molecular precursor *via* the phosphidation of the Co_3O_4 intermediate. The efficient construction of heterostructure through the variation of the surface/bulk composition significantly alters the interfacial properties and the electronic structure, yielding enhanced performance. Further, gas-phase phosphidation entails a core–shell phase formation mechanism *via* gas diffusion regulated by the Kirkendall effect. The optimized heterostructure (y=0.10) exhibits remarkable interfacial properties derived from the $CoO/Co^0/CoP$ interface, thus facilitating a high specific capacitance (466 F g^{-1} at 5 A g^{-1}) and excellent cycling stability (~91% after 10000 cycles) at 30 A g^{-1}. A further increase in the cyclability (~107%) was achieved by employing a graphene hybrid. Further, an asymmetric supercapacitor device was fabricated, that delivers a high energy density of 12.7 Wh kg^{-1} at a power density of 370 W kg^{-1} and cycling stability ~93% of the initial energy after 10000 cycles. This study reports on the modulation of the interfacial properties of CoP_x/CoO heterostructure to enhance energy storage performance *via* bulk/surface compositional variation, thereby providing a strategy to develop heterostructured electrodes for high-performance supercapacitor.

2

1. Introduction

The need for the development of eco-friendly and sustainable electrochemical energy storage devices, *viz.*, batteries and supercapacitors, has received substantial attention owing to the rapid depletion of natural resources and the rise in global warming.[1] Among them, supercapacitors are the most promising energy storage devices because of their fast charge–discharge property, high power density, good rate capability, and long cycle life.[2, 3] Battery-type electrodes (NiO, Co_3O_4, $Ni(OH)_2$) exhibit superior charge-storage behavior in supercapacitors compared to that of pseudocapacitive (MnO_2) and electric double layer capacitor (EDLC; carbon) materials; this is because of their high theoretical capacity, fast redox activity, and excellent electronic conductivity.[4] Nevertheless, battery-type electrodes exhibit poor cycle life and low Faradaic behavior. Thus, multi-component electrodes have been demonstrated to be ideal alternatives for augmenting charge storage by exploiting complementary properties of the components. Particularly, heterostructures formed by multi-component electrodes offer novel interfacial properties, unique electronic structures at the interface, and synergistic effects of discrete units, yielding enhanced energy storage for supercapacitor devices.[5-7]

Transition metal phosphides (TMP), particularly cobalt phosphide, have been widely explored as electrocatalysts for the oxygen evolution reaction (OER) owing to the electronic richness of the metal surfaces of phosphides.[8] Recently, TMP have gained attention for application as a promising electrode in supercapacitors; notably, this is because of their metalloid behavior, exceptional electronic conductivity, and rich redox reaction kinetics in alkaline media.[7] Thus far, reports on TMP phosphide (CoP, Ni_2P) electrodes for supercapacitors have been sparse owing to the poor structural stability of such electrodes.[9, 10]

3

Alternative electrodes, *viz.*, transition metal oxides, specifically CoO, yield a high theoretical

capacitance (~4000 F g^{-1})[11] and structural stability; further, they are abundant and economical.

Nevertheless, they are largely hindered by poor electrical conductivity.[12, 13] For instance,

cobalt phosphide has superior electronic conductivity (3.17 S cm^{-1}) compared to Co_3O_4 (10^{-4} to

10^{-2} S cm^{-1}).[14] Hence, the development of multi-component electrodes by hybridizing

conductive metal phosphides and metal oxides with high theoretical capacitance can produce

complementary properties, synergistic effects, and unique interfacial/electronic properties

beneficial for fabricating efficient supercapacitors.[15] Recently, a CoP_x/CoO hybrid catalyst

has been reported as a high-efficiency bifunctional electrocatalyst for lithium–air battery. This

is based on the ensemble effect of the exceedingly OER-active CoP and highly active CoO

catalysts that promote the oxygen reduction reaction (ORR).[12] Moreover, enhanced catalytic

activity was attained through the efficient modulation of electronic structure by lateral coupling

of components derived from a layered double hydroxide precursor.[16] This study focused on

the structural design and related aspects of Li–air batteries; however, it neglected the effect of

the compositional variation of each component on electrocatalytic performance. Despite a lack

of reports on CoP_x/CoO-based hybrids for supercapacitors, it is expected that the compositional

engineering of such hybrids would significantly broaden the scope for further advancement in

energy storage performance.

Zeolitic imidazolate frameworks (ZIFs), an important subclass of metal–organic frameworks

(MOFs), have gained interest owing their unique framework and robust structural, chemical,

and thermal stability; further, they have been demonstrated to be promising precursors for

transition metal-based energy materials.[17] A ZIF consists of transition metal centers (Zn, Co)

tetrahedrally linked to an imidazole organic linker, and it can exhibit myriad structural

variations, dimensionalities (2D/3D), and morphological features (cube, leaf-like, polyhedron).[17] Substantial effort has been focused on 3D ZIF precursors [ZIF-8(Zn), ZIF-67(Co)] owing to their excellent stability, large surface area, rich porosity, and unique polyhedron morphology.[18, 19] However, 3D ZIF-derived nanostructures exhibit relatively low electron transport because of high dimensionality and poor interparticle connectivity due to the intrinsic limitations of their morphologies. Post-treatment preserves the structural features of the ZIF precursor in the derived electrode material; furthermore, it creates hollow features, yielding fast mass transfer and exposed active sites, thereby boosting the energy storage capacity.[20] In contrast to 3D ZIF-derived hybrid, 2D ZIFs (particularly ZIFs with a leaf-like morphology that are made of Zn/Co) can possess a favorable 2D layered structure with a large surface area, facile electron transport, high utilization of active sites, and a leaf-like morphology (such ZIFs are denoted as ZIF-L, where L refers to a leaf-like morphology).[20] The construction of heterostructures on 2D layered structures facilitates lateral coupling, efficient interface formation, and favors synergism, thereby promoting the energy storage performance of 2D-ZIF-derived heterostructures.

Herein, we constructed a Co-based hybrid heterostructure to modify the electronic structure of the electrode material and enhance the energy storage capacity of supercapacitors. A CoP$_x$/CoO heterostructure with a leaf-like morphology was synthesized from a two-dimensional (2D) Co-based ZIF (ZIF-Co-L) as a molecular precursor *via* low-temperature two-step phase transformations: oxidation (Co$_3$O$_4$ intermediate) and controlled phosphidation. An effective reduction in the heterojunction resistance was realized through the controlled phase transformation of the ZIF-Co-L molecular precursor under varied proportions of phosphorous. Consequently, a remarkable charge-storage performance for supercapacitors was achieved. The

5

unique structure and morphological features facilitate access to electroactive sites and good contact with the electrolyte, significantly enhancing the capacitance and durability upon cycling. Besides, a graphene-based heterostructure with the graphene encapsulation of 2D leaf-like CoP_x/CoO was fabricated to enhance cycling stability. Further, an asymmetric supercapacitor device with a CoP_x/CoO heterostructure was fabricated. This device exhibited superior energy density with a high cycling stability, which is attributed to the interfacial and synergistic effect of the CoP_x and CoO components of the heterostructures.

2. Experimental section

2.1 Materials

Cobalt nitrate hexahydrate (98%), 2-methylimidazole (99%), poly(vinylideneflouride), and potassium hydroxide (reagent grade), zinc nitrate hexahydrate (98%), and carbon cloth were purchased from Sigma-Aldrich. Graphene oxide was purchased from Standard Graphene, South Korea. Acetylene black was purchased from Denka, Japan. Further, n-methylpyrrolidone (ACS grade) and methanol (pure grade) were purchased from Duksan Pure Chemicals, South Korea. All the chemicals were used as received without any further purification. Millipore water was used for all the experiments.

2.2 *Synthesis of the ZIF-Co-L and ZIF-Co-L/GO precursors.* The ZIF-Co-L precursor was synthesized using aqueous solutions of cobalt nitrate and 2-methylimidazole (mIm) with a mIm to Co ion molar ratio of 8. In a typical procedure, 2 mmol of $Co(NO_3)_2 \cdot 6H_2O$ and 16 mmol of mIm were dissolved separately in 45 mL of DI water. Then, the two solutions were mixed by stirring for 3 h. The as-obtained product was then washed with DI water five times, collected *via* centrifugation (8000 rpm/2 min), and dried overnight at 70 °C to obtain violet-colored crystals. The ZIF-Co-L/graphene oxide composite (ZIF-Co-L/GO) was synthesized by

6

dissolving the same molar ratio of Co/mIm in 40 mL of DI water, which was followed by the immediate addition of 10 ml of GO solution (0.0873 g of GO in 10 ml of DI water). The mixture was then stirred for 3 h and the subsequent procedures were similar to that for the pristine ZIF-Co-L precursor. The weight ratio (wt%) of cobalt nitrate to GO was fixed at 1:10, for the GO composite.

2.3 *Synthesis of the Co_3O_4-L and Co_3O_4-L/GO intermediates*. Co_3O_4-L was synthesized through the calcination of ZIF-Co-L at 400 °C for 2 h in air, at a heating rate of 1 °C min^{-1}. To synthesize the Co_3O_4-L/GO composite, a two-step heating method was employed. First, the GO in the ZIF-Co-L/GO was reduced to RGO. This was followed by its conversion to the oxide, Co_3O_4-L. ZIF-Co-L/GO was heated at 700 °C for 10 min under an Argon atmosphere at a heating rate of 5 °C min^{-1} for the reduction of GO. Subsequently, the heat-treated ZIF-Co-L/GO was calcined at 400 °C for 2 h in air at a rate of 1 °C min^{-1} to obtain Co_3O_4-L/GO.

2.4 *Synthesis of the CoP_x/CoO and CoP_x/CoO-RGO heterostructures*. CoP_x/CoO and CoP_x/CoO-RGO were obtained by *in-situ* selective phosphidation of the Co_3O_4-L and Co_3O_4-L/GO precursors, respectively. The phosphidation reaction was performed by placing Co_3O_4-L and NaH_2PO_2 (phosphorous source) in two separate alumina boats inside a tubular furnace; the NaH_2PO_2 boat was positioned upstream to induce a reaction between the solid Co_3O_4-L and the evolved PH_3 gases from the NaH_2PO_2 precursor. The samples were then heated at 350 °C for 2 h at a heating rate of 2 °C min^{-1} under an Argon atmosphere. Then, the samples were cooled to ambient temperature (25 °C). The cobalt phosphide and cobalt oxide phases in the heterostructure were regulated by altering the quantity of the phosphorous (NaH_2PO_2) precursor in the phosphidation process. Three different phosphorous contents were employed at variable

7

weight ratios of Co_3O_4-L to NaH_2PO_2, namely 1:20, 1:40, and 1:100 wt%, and the resulting product was labelled as CoP_x/CoO-wt% of P and the labels are abbreviated as CP_x/CO-20, CP_x/CO-40, and CP_x/CO-100, respectively. The CoP_x/CoO-RGO composite was prepared by phosphodizing Co_3O_4-L/GO with 40 wt% of NaH_2PO_2, denoted as CoP_x/CoO-40-RGO and abbreviated as CP_x/CO-40-RGO.

2.5 *Synthesis of N-doped porous carbon@graphene (NPC@rGO) sheets as the negative electrode for an asymmetric supercapacitor device*. NPC@rGO was synthesized from a $Zn_{0.9}$-$Co_{0.1}$-ZIF@GO precursor (consisting of 10 wt% of Co nitrate and 90 wt% of Zn nitrate) that was calcined at 800 ^{o}C in an argon atmosphere. Further, 0.329 g of $Zn(NO_3)_2 \cdot 6H_2O$ and 0.037 g of $Co(NO_3)_2 \cdot 6H_2O$ were dissolved concurrently in 12 ml of methanol, and 0.811 g of mIm was dissolved in 20 ml of methanol. The metal nitrate and mIM solutions were combined to obtain a clear solution. Then, 8 ml of the GO solution (composed of 1 mg ml^{-1} in water/methanol, 1:4 v/v) was added to the above solution mixture and stirred for 3 h. After stirring, a grey powder was collected by centrifugation and washed with methanol five times. The samples were dried at 50 ^{o}C overnight and denoted as $Zn_{0.9}$-$Co_{0.1}$-ZIF@GO. The $Zn_{0.9}$-$Co_{0.1}$-ZIF@GO precursor was further calcined at 800 ^{o}C for 5 h in an argon atmosphere. Then, the obtained carbon composite was immersed in 2 M HCl aqueous solution for 12 h and collected by centrifugation and washing with water multiple times. The samples were dried at 80 ^{o}C overnight, and the finally obtained sample was denoted as NPC@rGO.

2.6 *Electrochemical characterizations:* The electrochemical analysis of the samples was conducted by coating the synthesized active materials (80 wt%), acetylene black (10 wt%), and poly(vinylidenefluoride) (10 wt%) onto a carbon cloth substrate with an area of ~1 cm^2 and then dried at 100 °C for 12 h. The mass loading of the active material was maintained in the

8

range of ~2.2 to 2.8 mg cm^{-2}. Electrochemical studies were performed using a three-electrode system with a Pt plate and Hg/HgO as the counter electrode and reference electrode, respectively, in a 2 M aqueous KOH electrolyte. The electrochemical measurements, namely, cyclic voltammetry (CV), galvanostatic charge–discharge (GCD) measurements, and electrochemical impedance spectroscopy (EIS), were carried out on a PARSTAT electrochemical workstation. EIS was performed in the frequency range of 10^5 to 0.01 Hz, with an AC potential amplitude of 5 mV. The specific capacitance (C_m, F g^{-1}) of the electrode was calculated based on the galvanostatic charge–discharge curves using the following equation:[21]

$$C_m = \frac{I \times \Delta t}{m \times \Delta V} \tag{1}$$

where I (A) is the discharge current, Δt (s) is the discharge time, ΔV (V) indicates the potential window, and m (g) is the mass of the active material.

The asymmetric supercapacitor device was fabricated based on a two-electrode assembly comprising the synthesized CoP$_x$/CoO-40 active material and NPC@rGO as the positive and negative electrodes, respectively; the device was then tested using the 2 M KOH electrolyte. The mass loading of the positive and negative electrodes of the two-electrode device was optimized based on equation (2).

$$\frac{m+}{m-} = \frac{C_- \times \Delta V-}{C_+ \times \Delta V+} \tag{2}$$

The energy density (E) and power density (P) of the two-electrode cell were calculated using equations (3) and (4), respectively.[22]

$$E = \frac{C_m \times \Delta V^2}{7.2} \tag{3}$$

$$P = \frac{E \times 3600}{\Delta t} \tag{4}$$

9

2.7 *Materials characterization:* Powder X-ray diffraction (PXRD) of the samples was performed using a 3D-High-resolution EMPyrean/PANalytical XRD analyzer with Cu Kα radiation at a step size of 0.01° and a Bragg's angle range of $10° \leq 2\theta \leq 100°$; each sample was measured for 1 h. Rietveld refinement was performed using FullProf Suite.[23][24] The refined instrumental parameters were zero point displacement and background. The refined structural parameters for all phases were scale factor, unit cell parameters, and the peak profile based on the Thompson–Cox–Hastings pseudo-Voigt (TCHpV) profile parameters.[24] The instrumental resolution was considered by refining the TCHpV profile parameters for the Si standard and including them in an instrumental resolution file (*.irf) employed in the refinements. The initial model for the Rietveld refinement of the CoP, Co_2P, and CoO phases was obtained from relevant literature.[25-27] For analyzing the nanostructure of the samples, field emission-scanning electron microscopy (FE-SEM) and high-resolution transmission electron microscopy (HR-TEM) were performed using a Hitachi S-4800 and FEI Tecnai F20 (200 kV), respectively, at the Korea Basic Science Institute (KBSI), Gwangju center, South Korea. Laser Raman spectra were also collected at KBSI using a Horiba Jobin Hyon ARAMIS with backscattering geometry. X-ray photoelectron spectra (XPS) measurements were performed using a VG Multilab 2000 with Al as the target anode for X-ray generation. The X-ray photon energy (Al Kα) was 1480 eV, with a line width of 0.5 eV. Moreover, Fourier transform infrared (FT-IR) measurements were recorded using a PerkinElmer Spectrum 400 with KBr pellets, in a wavenumber range of 400 to 4000 cm^{-1}, at the Centre for Development of Fine Chemicals (CDFC), Chonnam National University, South Korea. The Brunauer–Emmett–Teller (BET) specific surface area was determined *via* nitrogen adsorption–desorption at 77 K on a Belsorp mini analyzer.

3. Results and discussion

The general synthesis strategy for fabricating a leaf-like CoP_x/CoO heterostructure is illustrated in **Figure 1a**. The CoP_x/CoO heterostructure was synthesized using a metastable 2D leaf-like Co-based ZIF-Co-L molecular precursor as a sacrificial template *via* a two-step phase transformation process: calcination to Co_3O_4-L and a consequent controlled phosphidation step. The typical synthesis involved a simple self-assembly approach using the reaction of $Co(NO_3)_3 \cdot 6H_2O$ and 2-methylimidazole in an aqueous solution at room temperature to yield a violet-colored precipitate of the ZIF-Co-L precursor. The organic imidazolate molecules act as a bridging ligand to chemically coordinate the cobalt ions through a self-assembly approach, thus forming the ZIF framework, which serves as a molecular precursor. Note that ZIF-Co-L, a metastable phase, can only be formed when the molar ratio between the organic linker and Co ions is ≤8; when this ratio is exceeded, the leaf-like ZIF-Co-L transforms to stable polyhedrons of ZIF-67 with a completely different structure and morphology.[28] The GO-draped ZIF-Co-L composite was synthesized using a similar procedure, except for the addition of the GO solution, which favored a strong binding interaction between the Co ions of the ZIF-Co-L framework and the oxygen sites of the GO (**Figure S1a, Supporting information**). The successful formation of ZIF-Co-L was confirmed *via* PXRD, which confirmed the high crystallinity of the sample, as shown in **Figure 1b;** this is in good agreement with previously reported results regarding ZIF-Co-L.[29] Furthermore, ZIF-Co-L is a 2D layered cobalt imidazolate framework with the composition $Co(mIm)_2$-$(HmIm)_{1/2}(H_2O)_{3/2}$ that forms unique cushion-shaped cavities comparable to its parent, ZIF-Zn-L.[28, 30] Identical diffraction patterns were obtained for the ZIF-Co-L and ZIF-Co-L/GO precursors, indicating that the ZIF-Co-L crystal structure is well

11

preserved in the presence of GO (**Figure S1b, Supporting information**). The ZIF-Co-L molecular precursor was then converted to its oxide *via* calcination in air at 400 °C at a slow heating rate of 2 °C min^{-1}. The PXRD pattern of the oxide product shows the characteristic diffraction peaks of the cubic Co_3O_4 structure (**Figure 1c**). The Co_3O_4 forms a spinel structure with Co^{3+} ions in the distorted octahedral (CoO_6) coordination and Co^{2+} ions in the tetrahedral (CoO_4) coordination in a cubic close-packed lattice of oxide ions. The graphene feature at 26° cannot be seen in Co_3O_4-L/GO, which may be due to the unreduced GO sheets and increased oxygen functional groups on the GO sheets during thermal annealing in air (**Figure S1c, Supporting information)**. Furthermore, the morphologies of the as-obtained ZIF-Co-L and Co_3O_4-L precursors were analyzed using FE-SEM and TEM. The ZIF-Co-L framework exhibited a 2D leaf-shaped morphology, with lengths ranging from ~2 μm to several μm and a thickness of ~210 nm, as shown in **Figure 1d, e**. A considerable decrease in the lengths of the ZIF-Co-L leaves (≤1 μm) was observed in the presence of GO **(Figure S1f, Supporting information)**; this indicates the size-controlling effect due to the homogenous anchoring of leaf-shaped microcrystals on the GO surface. The leaf-shaped morphology was preserved in the oxide phase after thermal annealing of the pristine ZIF-Co-L and ZIF-Co-L/GO composite, (**Figure S1g-h, Supporting information**). Similarly, Co_3O_4-L/GO exhibited a smaller leaf structure (≤250 nm) than that observed in Co_3O_4-L; this was owing to the evaporation of H_2O and CO_2 molecules from the GO, the decomposition of organic linkers from the ZIFs of ZIF-Co-L/GO, and the lower surface roughness of the GO sheets due to the air annealing effect. The highly crystalline nature of Co_3O_4-L was reaffirmed by the bright spots observed through selected area electron diffraction (SAED); further, a diffused line observed in the case of

12

Co_3O_4-L/GO indicates its nanocrystalline nature, which arises from the smaller leaf crystals that occur in the presence of GO (**Figure S2, Supporting information**).
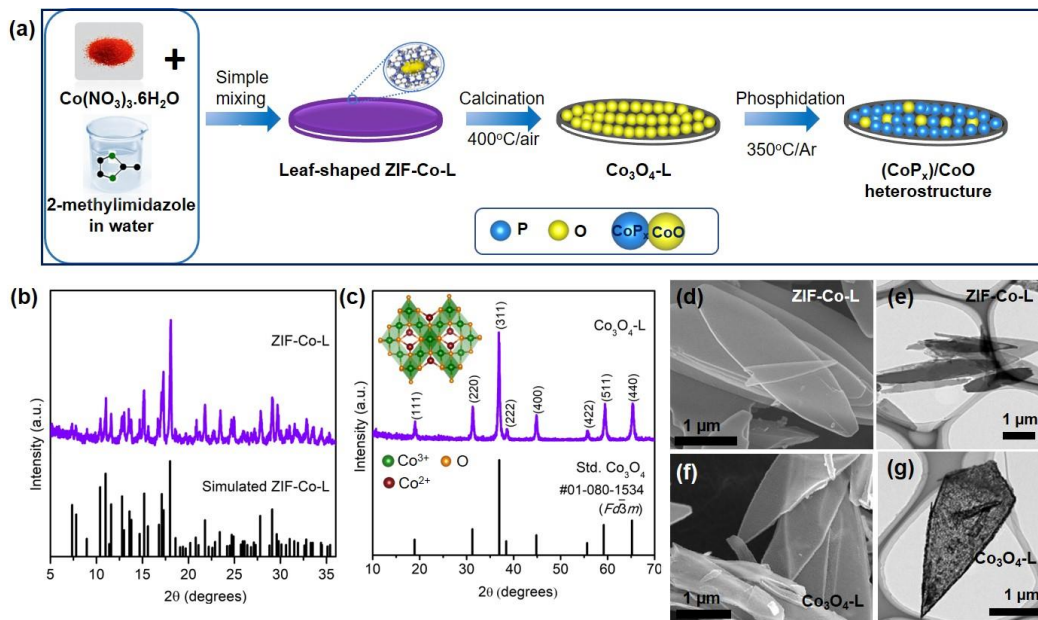
Figure 1. Synthesis scheme of leaf-shaped CoP_x/CoO and structural analysis of precursors. (a) Scheme for synthesis of CoP_x/CoO heterostructures; Powder XRD of (b) ZIF-Co-L and (c) Co_3O_4-L precursors; (d) SEM and (e) TEM of ZIF-Co-L precursor; (f) SEM and (g) TEM images of Co_3O_4-L precursor.

Consequently, selective phosphidation of the Co_3O_4-L intermediate, performed by low-temperature calcination at 350 °C in the presence of sodium hypophosphite ($NaH_2PO_2·H_2O$), resulted in the formation of the CoP_x/CoO heterostructure. Typically, a phosphidation reaction with NaH_2PO_2 proceeds through a solid–gas reaction between solid Co_3O_4-L and PH_3 gas (P precursor) generated during the thermal decomposition of NaH_2PO_2 at 350 °C.[31] Composition engineering of the phosphide and oxide phases was performed by regulating the weight ratios of the $NaH_2PO_2·H_2O$ and Co_3O_4-L precursors. Note that high-temperature phosphidation (>400 °C)

13

would result in complete conversion to the phosphide (CoP, Co_2P) phase, rather than the desired mixture of the oxide and phosphide phases.[32] The weight ratios between Co_3O_4-L and $NaH_2PO_2 \cdot H_2O$ were altered to perform controlled phosphidation: Three different weight ratios were employed, *viz.*, 1:20, 1:40, and 1:100 wt%, and the obtained products were labeled as CP_x/CO-20, CP_x/CO-40, and CP_x/CO-100, respectively, denoting a CoP_x/CoO heterostructure. Likewise, a graphene (RGO)-draped CoP_x/CoO heterostructure was derived *via* the phosphidation of the Co_3O_4-L/GO intermediate. The influence of the phosphorus precursor on the crystal structure, at varied weight ratios, was analyzed using PXRD and is shown in **Figure 2a.** The PXRD patterns of the phosphorized products are completely different from those of the initial Co_3O_4-L precursor, suggesting the complete transformation of the Co_3O_4-L into a new product. Furthermore, the characteristic peaks of orthorhombic CoP (space group, SG: *Pnma*), orthorhombic Co_2P (SG: *Pnma*), and cubic CoO (SG: $Fm\bar{3}m$) were evident, implying the conversion of the Co_3O_4-L to a mixture of the Co-P (CoP, Co_2P) and CoO phases. In the orthorhombic CoP structure, CoP_6 octahedra in which Co^{3+} is edge-shared with neighboring octahedra are formed, whereas CoO adopts a cubic phase, forming CoO_6 octahedra where Co^{2+} is corner-shared with neighboring octahedra (**Figure 2b**). As the P precursor amount increased during phosphidation, the phosphide (CoP, Co_2P) phase formation dramatically escalated, leading to a dominant CoP_x (CoP+Co_2P) phase while significantly reducing the oxide (CoO) phase. The quantification of the CoP, Co_2P, and CoO components would provide insights into the role of each component and the corresponding phase-driven supercapacitive properties. Hence, Rietveld refinement was performed on the PXRD data, and phase fractions of individual components were estimated and presented in **Figure 2b** (**Figure S3**, **Supporting information**). The refinement studies ascertained the increase in the CoP_x phase from 56% to 94% and the

14

decrease in the phase fraction of the CoO material (from 44% to 6%) when the P precursor is increased from 20 to 100 wt%, as shown in **Figure 2c** (**Table S1, S2, Supporting information**). Nevertheless, in the estimated CoP_x phase ($CoP + Co_2P$), the proportion of the P-deficient Co_2P phase remained ≤9% in all the samples. Hence, for simplicity, the combined phase fraction of the dominant CoP and minor Co_2P phases is described as CoP_x, where the estimated x is ≤0.9. The phosphodired samples with varying ratios of Co_3O_4-L to $NaH_2PO_2 \cdot H_2O$, namely 1:20, 1:40, and 1:100 wt%, are described based on their phosphorous content and as the CP_x/CO-20, CP_x/CO-40, and CP_x/CO-100, respectively. The estimated bulk compositions of the phosphorized CP_x/CO-20, CP_x/CO-40, and CP_x/CO-100 samples are $(CoP_x)_{0.56}$/$CoO_{0.44}$, $(CoP_x)_{0.90}$/$CoO_{0.10}$, and $(CoP_x)_{0.94}$/$CoO_{0.06}$, respectively. The CP_x/CO-20 sample displayed nearly equivalent phase fractions of CoP_x and CoO, namely, 56% and 44%, respectively. Upon increasing the P source to 40 wt% (CP_x/CO-40), an abrupt increase in CoP_x to ~90% was observed, and merely 10% of the CoO phase remained. Notably, when the amount of the P source was more than doubled to 100 wt% (CP_x/CO-100), the proportion of CoP_x remained high, at ~94%, with the remaining 6% corresponding to the CoO phase. Thus, the oxides were not completely converted to phosphides, even with greater amounts of the P precursor than those reported in the literature. This is due to the robust structural features of the leaf-shaped ZIF-Co-L precursor that preserved the deeply integrated oxide phase in Co_3O_4-L, thereby hindering PH_3 gas penetration *via* the gas-induced phosphidation process. Any further increase in the P precursor amount leads to a poor synthesis yield, inadequate for PXRD analysis. The conversion of Co_3O_4-L (Co^{III}) to cobalt monoxide ($Co^{II}O$) during phosphidation is due to the strong reducing nature of PH_3 gas.[12] This assumption was also confirmed by annealing Co_3O_4 at 350 °C under an argon atmosphere in the absence of a NaH_2PO_2 source; notably, the Co_3O_4

15

phase was retained, without any formation of a CoO phase (reduced oxidic phase). The morphology of the phosphodired sample was analyzed using SEM. The SEM and TEM images showed that after phosphidation, the samples retained the leaf-like morphology of the Co_3O_4-L intermediate while forming well-integrated CoP_x and CoO nanoparticles on the robust leaf template. The average cross-sectional length × diameter of the CoP_x/CoO leaves is ~5 × 2 μm for CP_x/CO-20, which reduced further to ~4 × 1.4 μm in other samples with a higher P precursor amount. (**Figure S4, Supporting information, and Figure 2d**). The thickness of the leaf-like microcrystals is ~200 nm. Further TEM elemental mapping reaffirmed the presence of Co, P, and O in CoP_x/CoO and the uniform distribution of Co, P, and O, denoting laterally interconnected CoP and CoO particles on the leaf-like structure, was confirmed; thus, an ordered heterostructure was formed. This leaf-like microstructure with abundant CoP_x/CoO heterojunctions may provide rich interfaces and ample exposed active sites, which is expected to enhance the charge storage property. A substantial change in the distribution of O and P on the heterostructure was observed with an increase in P content, as shown in **Figure 2d-f**. Particularly, P was abundant at the surface in CP_x/CO-20, whereas O was abundant in the interior or bulk of the leaf structure, despite the homogeneous distribution of cobalt (**Figure 2d**). In the CP_x/CO-40 sample, obtained with a higher P source amount, the thickness of the P-rich region at the surface increased substantially, whereas O remained intact in the bulk (**Figure 2e**). This demonstrates that phosphidation of solids occurs from the surface to the bulk as P content increases. In the case of the highest P content (CP_x/CO-100), a homogenous distribution of P and O was apparent, with a slight increase in the oxygen isolates at the surface (**Figure 2f**). The differential distribution of P and O with an increase in the P content illustrates the core-shell mechanism of the phosphidation reaction controlled by the Kirkendall reaction.[33] Typically,
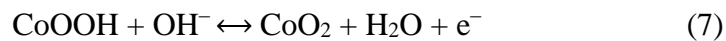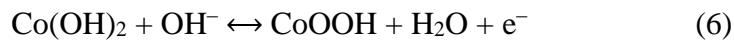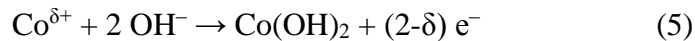
16

the phosphidation step involves the gasification of the NaH_2PO_2 precursor to PH_3 gas, which then reaches and becomes absorbed into the surface of the Co_3O_4-L precursor under an argon flow. The P tends to diffuse inward, whereas O diffuses outward, facilitating the reaction with the PH_3 gas; this drives the reaction through the chemical potential and concentration gradient.[34] Hence, CoP formation occurs from the surface to the bulk and is strongly dependent on the magnitude of the PH_3 precursor. Besides, the formation of substantially thick CoP at the surface may impede further phosphidation, which may be overcome by employing an excess of the NaH_2PO_2 precursor. However, the formation of oxygen-rich clusters or isolates on the surface of CP_x/CO-100 (**Figure 2f)** is anticipated based on the outward diffusion of O from the bulk, which causes strain-induced segregation in the CoP-rich region. Furthermore, the diffraction rings in the SAED result of CP_x/CO-40 were indexed with the planes of the CoP, Co_2P, and CoO phases **(Figure 2g)**. The TEM fringe spacings of 2.1 Å and 2.5 Å correspond to the (200) planes of CoP and CoO, respectively **(Figure 2h-i)**.
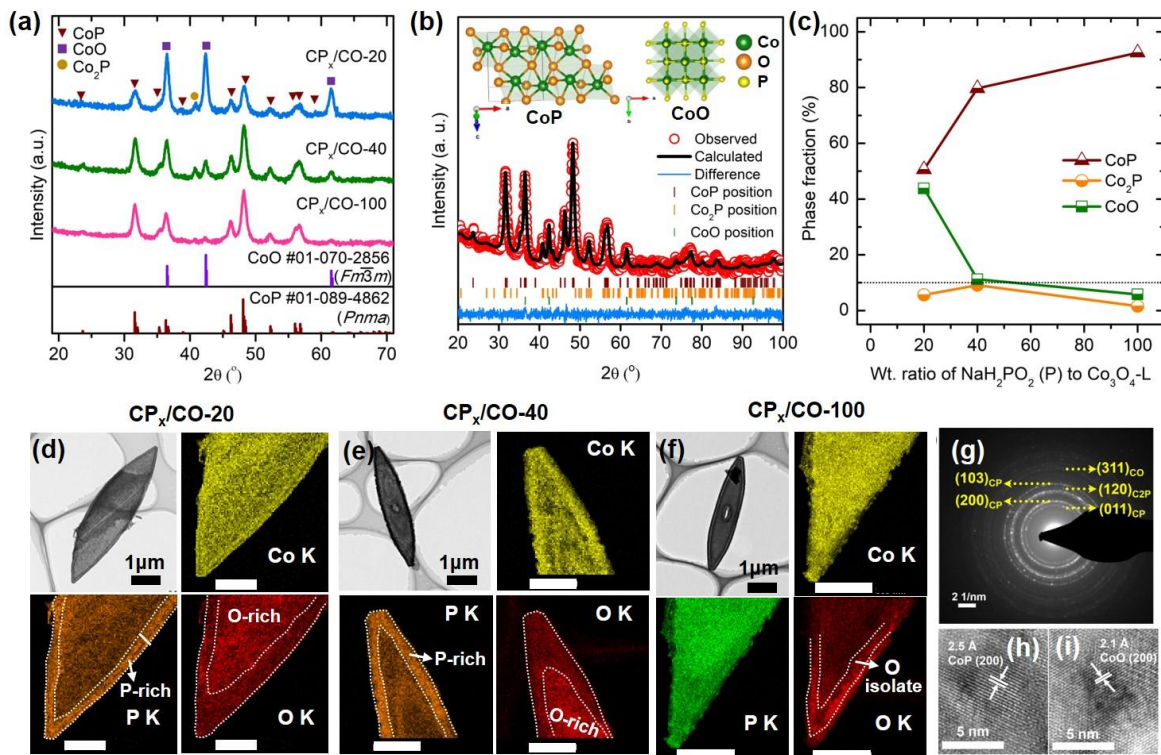
Figure 2. Structural evaluation of phosphorous-varied CoP$_x$/CoO heterostructures. (a) PXRD of CoP$_x$/CoO with varying weight (wt.) ratios of precursors NaH$_2$PO$_2$ and Co$_3$O$_4$-L from 20–100 wt%. (b) Rietveld refinement XRD result for CP$_x$/CO-40; the insets depict the crystal structures of the orthorhombic CoP and cubic CoO phases. (c) Phase fractions of CoP, Co$_2$P, and CoO with varying phosphorous content; TEM and elemental mapping (Co, P, O) of (d) CP$_x$/CO-20, (e) CP$_x$/CO-40, and (f) CP$_x$/CO-100, (g) SAED pattern of CP$_x$/CO-40, lattice fringes corresponding to (h) CoP and (i) CoO phases. The CoP, Co$_2$P, and CoO phases are denoted as CP, C2P, and CO in the SAED phase indexing. The scale bar in Figure 2(d-f) represents 500 nm.

The charge storage performance of the composition-engineered CoP$_x$/CoO heterostructure was evaluated in 2 M KOH electrolyte and compared with that of Co$_3$O$_4$-L. The CV results in the potential range of 0 to 0.55 V *vs.* Hg/HgO exhibited a significantly higher integral area for CoP$_x$/CoO, compared to that for Co$_3$O$_4$-L; moreover, distinct oxidation/reduction peaks signifying dissimilar faradaic processes were observed (**Figure 3a**). The specific capacitance of

CoP$_x$/CoO, derived from the GCD profile, is 467 F g^{-1} at 5 A g^{-1}, which is substantially higher than that of Co$_3$O$_4$-L with 35 F g^{-1} (**Figure S5, Supporting information**). The phase conversion of Co$_3$O$_4$-L to the CoP$_x$/CoO heterostructure *via* controlled phosphidation led to an enhanced enclosed CV area. The enhanced specific capacitance of CoP$_x$/CoO was attributed to the high redox activity of CoP and the interfacial properties of the formed heterostructure. CV of the CoP$_x$/CoO electrode was also performed across a wide potential range, from -0.1 to 0.6 V; the results reveal two pairs of redox couples with three anodic peaks at 0.02 V and two pronounced peaks at 0.18 V and 0.53 V *vs.* Hg/HgO (**Figure S6, Supporting information**). The peak at 0.02 V corresponds to the oxidation of CoP (Co$^{\delta+}$) to Co(OH)$_2$ (equation 5), and the last two peaks at 0.018 and 0.48 V can be attributed to the transformation of Co(OH)$_2$ into CoOOH (equation 6) and the subsequent transformation of CoOOH into CoO$_2$ (equation 7), respectively:[9]

$$Co^{\delta+} + 2\ OH^- \rightarrow Co(OH)_2 + (2\text{-}\delta)\ e^- \qquad (5)$$

$$Co(OH)_2 + OH^- \leftrightarrow CoOOH + H_2O + e^- \qquad (6)$$

$$CoOOH + OH^- \leftrightarrow CoO_2 + H_2O + e^- \qquad (7)$$

The phosphidation process elevates the electrochemical performance of the CoP$_x$/CoO heterostructure. The composition engineering of the CoP$_x$/CoO heterostructures is expected to alter their electrochemical properties owing to variations in the individual CoP$_x$ and CoO components and tunable bulk/interfacial properties. The electrochemical activity of the composition engineered CoP$_x$/CoO heterostructures was investigated and presented in **Figure 3**. The enclosed area of the CV curve measured at 30 mV s^{-1} increases with an increase in CoP$_x$ content from 56% in CP$_x$/CO-20 to 90% in CP$_x$/CO-40; however, it subsequently decreases in the case of the CP$_x$/CO-100 sample with 94% of CoP$_x$ (**Figure 3a**). The lowest integral CV area

was observed for CP_x/CO-20, which may be due to its higher CoO content, ~44% ($CoP_x = 56\%$), compared to that of the other samples; note that CoO is a poorer conductor than CoP. CP_x/CO-40 attained the highest performance, which was anticipated owing to the presence of the dominant CoP (~90%) phase. However, CP_x/CO-100 with a slightly higher CoP phase fraction (94%) exhibited an abnormally low enclosed CV area. Hence, the integral CV curve area follows the trend of CP_x/CO-40 > CP_x/CO-100 > CP_x/CO-20, which is independent of the bulk phase fraction of conducting CoP in the corresponding samples, that is 90% →94% →56%, respectively. The electrochemical performance is apparently dependent on the phase fraction of conducting CoP in CP_x/CO-20 and CP_x/CO-40; however, CP_x/CO-100 deviates from the anticipated trend owing to the formation of surface oxygen or insulating CoO isolates, as observed from TEM (**Figure 2f**). In addition, the highest CV integral area, obtained for CP_x/CO-40 with a bulk composition of $(CoP_x)_{0.90}$/$CoO_{0.01}$, may be due to the anticipated interfacial properties of the well-integrated CoP_x/CoO heterostructure. This trend in the charge storage property was also evident from the GCD profiles obtained at a high current density (30 A g^{-1}), as shown in **Figure 3b**, suggesting the effect of the composition (bulk/surface) and the interfacial property of the heterostructure. The IR drop trend observed from the GCD results is inversely related to the integral CV area (**Figure 3a**), signifying that a lower IR drop leads to a higher CV area and enhanced charge storage property. These results suggest that electrochemical activity can be altered rationally by varying the composition (surface/bulk) of the CoP_x/CoO heterostructure, which in turn modulates the interfacial properties. **Figure 3c** depicts the CV curves of the CP_x/CO-40 heterostructure at variable scan rates in a wide potential window of -0.1 to 0.6 V. The shape of the CV curves was retained upon increasing the scan rates, and the oxidation and reduction (Faradaic reaction) peaks shifted to slightly higher

20

and lower potentials, respectively, signifying the diffusion-controlled reaction kinetics and high reversibility of the electrode material with low internal resistance. Besides, the CV curves of the CP_x/CO-20, CP_x/CO-40, and CP_x/CO-100 heterostructures at different scan rates in the potential range of 0 to 0.55 V showed a similar trend in the enclosed area (**Figure S7, Supporting information**). The GCD profiles of the CP_x/CO-40 electrode were obtained at different current densities (5 to 30 A g^{-1}) in the potential range of 0 to 0.55 V (**Figure 3d**). The GCD plots depict a symmetric charge–discharge profile, indicating good reversibility of the CP_x/CO-40 electrode. For comparison, the GCD plots of the CP_x/CO-20 and CP_x/CO-100 electrodes were also obtained (**Figure S8, Supporting information**). **Figure 3e** depicts the specific capacitance of the CoP_x/CoO electrodes, derived from GCD curves as a function of current density. A similar specific capacitance trend was observed based on the CV area and GCD plots (**Figure 3a, 3b**). The results confirmed that the CP_x/CO-40 electrode delivered a higher specific capacitance than the CP_x/CO-20 and CP_x/CO-100 electrodes. The CP_x/CO-40 electrode exhibited a superior specific capacitance of 467 F g^{-1}, compared to those of CP_x/CO-20 (359 F g^{-1}) and CP_x/CO-100 (412 F g^{-1}), at 5 A g^{-1} with a reasonably good rate capability. These results signify the successful tuning of the electrochemical activity of the heterostructure by regulating the CoP_x/CoO ratios, eventually modulating the electronic structure. The specific capacitance of the optimized CoP_x/CoO-40 heterostructure (467 F g^{-1} at 5 A g^{-1}) is much superior to the capacitance reported for individual CoP, Co_2P, and CoO electrode-based supercapacitors (**Table 1**). Values from the literature were chosen based on the high-performance morphologies (solid, hollow, cubes, and flower structures) of CoP, Co_2P, and CoO electrodes, which have been developed to alter the surface area and ion diffusion to obtain enhanced supercapacitive performance. Wang *et al.*[21] proposed a unique solid CoP microcube with a specific

capacitance of 300 F g^{-1} at 5 A g^{-1} in Ni foam as a current collector and also fabricated hollow microcube structures to enhance the surface area, thereby achieving the highest reported capacitance of 485 F g^{-1} at 5 A g^{-1} for CoP electrodes (**Table 1**). Chen *et al.*[35] reported that Ni-foam-supported Co$_2$P nanorods and Co$_2$P nanoflowers delivered specific capacitances of 284 and 416 F g^{-1}, respectively, at 1 A g^{-1}. Further, Cheng *et al.*[36] demonstrated hollow Co$_2$P nanoflowers with a capacitance of 321 F g^{-1} at 1 A g^{-1}, which is lower than that achieved in the present work. Tang *et al.*[37] demonstrated that the rational design of porous CoO nanowalls grown on Ni foam structures enabled enhanced electrochemical performance, delivering a specific capacitance of 311 F g^{-1} at 5 A g^{-1}. The superior supercapacitive performance of the CoP$_x$/CoO lateral heterostructures compared to that of the individual (CoP, Co$_2$P, CoO) electrodes is attributed to the synergistic effect of the conducting CoP$_x$ and high capacitance CoO electrodes, as well as the interfacial properties of the heterostructure with an optimized composition.

EIS spectra were measured to evaluate the charge transfer kinetics at the electrode–electrolyte interface. The corresponding Nyquist plot exhibits a semicircle that represents the charge transfer resistance (Rct) determined from the intercept on the real axis, as shown in **Figure 3f**. The optimized CP$_x$/CO-40 heterostructure electrode exhibited the lowest charge transfer resistance (38 Ω) compared to the other electrodes [CP$_x$/CO-20 (62 Ω) and CP$_x$/CO-100 (59 Ω)]. This suggests that the enhanced conductivity and charge transfer kinetics of the optimized CP$_x$/CO-40 heterostructure were derived from the remarkable interfacial properties. The charge transfer resistance may depend on the CoP content because CoP is highly conductive. Thus, a higher CoP content may reduce the resistance, thereby enhancing the electronic conductivity. However, the charge transfer resistance of CP$_x$/CO-100 is higher than

22

that of CP$_x$/CO-40, although the former possesses more CoP (94%), which is attributed to surface-anchored oxygen isolates (**Figure 2f**). The excellent electrical conductivity of CP$_x$/CO-40 promoted its charge storage capability through enhanced electron transfer and redox reactions. This suggests that the presence of a considerable amount of CoP in the heterostructure would reduce the charge transfer resistance, along with the tuning of the interfacial properties, which also appreciably enhances the electronic conductivity of CoP$_x$/CoO electrodes.[12] Besides, it has been reported that the presence of an equivalent amount of CoO and CoP (in a ratio of 1:1) leads to the formation of oxygen–phosphorous (O–P) at the CoP–CoO interface, which increases the electrochemical activity owing to enhanced conductivity and electron transfer kinetics.[12] Nevertheless, in this study, the presence of a large amount of CoP (90%) in the CoP$_x$/CoO heterostructures, rather than an equivalent amount of CoP and CoO (50% each), yielded an enhanced charge storage performance by promoting the electronic conductivity and interfacial properties for supercapacitor applications.

Furthermore, to confirm the long-term practical applicability of the CoP$_x$/CoO heterostructure electrodes for supercapacitors, charge–discharge cycles were performed at a high current density of 30 A g^{-1} in a 2 M KOH electrolyte for 10000 cycles, as depicted in **Figure 3g**. All the heterostructure electrodes demonstrated a significant level of activation upon cycling, which is probably due to the slow diffusion of the electrolyte into the porous carbon cloth substrate due to delayed wettability. Hence, the capacitance at the 600th cycle was chosen as the initial capacitance to evade the influence of the activation process in the estimation of capacitance retention and cycling stability, which would lead to >100% retention. The CoP$_x$-rich CoP$_x$/CoO heterostructures, namely, CP$_x$/CO-40 and CP$_x$/CO-100, respectively retained 91% and 98% of the initial capacitance after 10000 cycles, affirming the outstanding

23

electrochemical stability of the CoP$_x$/CoO active material. In the case of CP$_x$/CO-20, cycle retention of 100% was observed after 10000 cycles. The higher cycle retentions (100% and 98%) of CP$_x$/CO-20 and CP$_x$/CO-100 compared to that of CP$_x$/CO-40 (91%) suggest the probable role of the oxidic (CoO) phase in cycling stability. The larger amount of CoO (44%) in CP$_x$/CO-20 resulted in a negligible capacitance loss after prolonged cycling, whereas in CP$_x$/CO-100, despite its lower CoO content (6%), surface oxidic (CoO) isolates could result in a higher cycling stability. Hence, it is relevant to conclude that the reduced cobalt oxidic (CoO) phase enhances cycling stability, whereas cobalt phosphide (CoP$_x$) contributes to a higher specific capacitance. In the CP$_x$/CO-40 heterostructure, in addition to the interfacial property, the optimized CoP$_x$ and CoO contents resulted in a higher capacitance (466 F g^{-1}) and promoted cycling stability (91% capacitance retention). These results demonstrate the excellent cycling stability of the CoP$_x$-rich CoP$_x$/CoO heterostructure electrodes for supercapacitors.

The relationship between the CoO$_{bulk}$ content and charge transfer resistance (EIS) is presented in **Figure 3h**. A decrease in the poorly conductive CoO$_{bulk}$ phase in the CP$_x$/CO-40 has reduced its charge transfer resistance than that of CP$_x$/CO-20. Further, the abnormal increase in the resistance of CP$_x$/CO-100 is attributed to the presence of surface CoO isolates. Besides, the unusual decrease in the charge transfer resistance of CP$_x$/CO-40 is attributed to its optimal interfacial properties, which enhance its charge storage property. Based on the results, the energy storage mechanism of CoP$_x$/CoO can be attributed to the faradaic redox reactions of CoP and CoO in a KOH electrolyte *via* the reversible faradaic reactions of the CoP/CoPOH and CoPOH/CoPO redox couples.[7] Moreover, the well-interconnected CoP$_x$ and CoO nanoparticles on the leaf-shaped precursor template avoid a high heterojunction resistance during the electrochemical reaction, accelerating the reaction kinetics; moreover, they offer

24

efficient synergy between CoP$_x$ and CoO, providing facile ion and charge transfer in the electrode and ensuring rich redox reactions.[7]
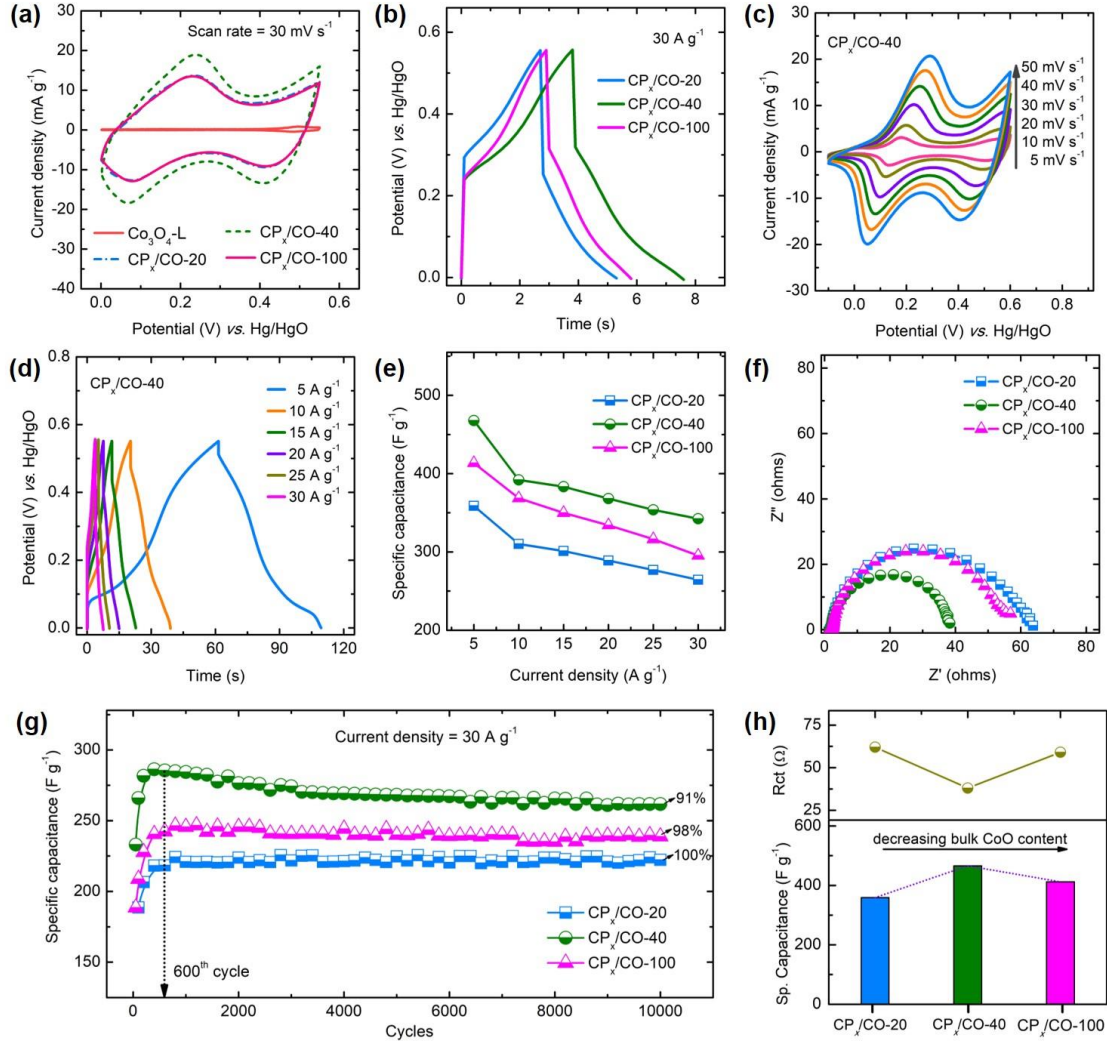
Figure 3. Capacitance behavior of the composition(y)-varied (CoP$_x$)$_{1-y}$/CoO$_y$ heterostructure by changing the phosphorous precursor. (a) CV of Co$_3$O$_4$ and (CoP$_x$)$_{1-y}$/CoO$_y$ electrodes at scan rate of 30 mV s^{-1}, (b) galvanostatic charge/discharge profiles of (CoP$_x$)$_{1-y}$/CoO$_y$ electrodes at 30 A g^{-1}; (c) CV of the CP$_x$/CO-40 at varying scan rates of 5 to 50 mV s^{-1}; (d) GCD profiles of CP$_x$/CO-40 at different current densities of 5 to 30 A g^{-1}; (e) specific capacitance of (CoP$_x$)$_{1-y}$/CoO$_y$ at different current densities; (f) electrochemical impedance spectra (EIS) of (CoP$_x$)$_{1-y}$/CoO$_y$ samples; (g) cycling stability of the (CoP$_x$)$_{1-y}$/CoO$_y$ at 30 A g^{-1}, where the cyclability is calculated from the 600th cycle; (h) relation between P-varied (CoP$_x$)$_{1-y}$/CoO$_y$ composition to the initial specific capacitance (600th cycle) and charge-transfer resistance (Rct, derived from EIS).

25

Table 1. Comparison of supercapacitive performance in a three-electrode system for state-of-the-art materials reported in the literature, for CoP, Co$_2$P, CoO electrodes. (CC - carbon cloth)

Electrode material	Electrolyte/ Substrate	Current density	Specific capacitance	Capacitance retention (%)	Reference
$(CoP_x)_{0.90}/CoO_{0.10}$	2 M KOH/ CC	5 A g^{-1}	467 F g^{-1}	91 (10000 cycles at 30 A g^{-1})	This work
Hollow CoP cube	6 M KOH/ Ni foam	5 A g^{-1}	485 F g^{-1}	91 (10000 cycles at 5 A g^{-1})	[21]
Solid CoP cubes	6 M KOH/ Ni foam	5 A g^{-1}	300 F g^{-1}	80 (10000 cycles at 5 A g^{-1})	[21]
Co$_2$P nanorods	6 M KOH/ Ni foam	1 A g^{-1}	284 F g^{-1}	---	[35]
Co$_2$P nanoflowers	6 M KOH/ Ni foam	1 A g^{-1}	416 F g^{-1}	---	[35]
Hollow Co$_2$P nanoflower	6 M KOH/ Ni foam	4 A g^{-1}	321 F g^{-1}	124 (10000 cycles at 5 A g^{-1})	[36]
Porous CoO nanowall	6 M KOH/ Ni foam	5 A g^{-1}	311 F g^{-1}	93 (5000 cycles at 10 A g^{-1})	[37]

To acquire additional insights into the surface composition, chemical states, and explication for the superior charge storage performance of the CoP$_x$/CoO heterostructure, the XPS were measured. **Figure 4a-c** represents the Co 2p, P 2p, and O 1s XPS of the CoP$_x$/CoO samples. The high-resolution Co 2p spectra were deconvoluted into two sets containing four peaks each, corresponding to the spin–orbit doublets of Co 2p$_{3/2}$ and Co 2p$_{1/2}$, in the binding energy (BE) ranges of 775–790 eV and 790–810 eV, respectively. The Co 2p peaks at 778.5 eV and 793.3 eV were assigned to the Co^{3+} of the CoP phase, which is blue-shifted compared to the metallic cobalt (778.2 eV) [38]; further, the peaks at 781.5 eV and ~797.5 eV are associated with Co^{2+},

indicating the coexistence of CoO.[15] Two sets of shake-up satellites were observed in the ranges of 784–786 eV and 800–805 eV.[32] It should be noted that the Co^{3+} (Co–P) peak shifted to a lower BE (778.2 eV) in CP_x/CO-40, which is ascribed to the partial reduction of Co^{3+} to metallic cobalt. The metallic cobalt formation may arise owing to the unique metallic states formed at the CoP_x/CoO interface with an appropriate composition, leading to the exceptional interfacial properties in the heterostructure. The metallic cobalt could significantly increase the electronic conductivity and improve the charge storage properties of CP_x/CO-40. The P 2p core spectra exhibit two peaks, *viz.*, the lower BE peak at ∼129.4 eV (overlapping of $2p_{3/2}$ and $2p_{1/2}$), associated with cobalt phosphide, and the higher BE peak at ∼133.4 eV, associated with surface oxidized P species (PO_x). This arises from the oxidation of the surface P species in contact with air, as shown in **Figure 4b**.[12, 15] An increase in the phosphide to PO_x ratio (P/PO_x), with an increasing P source amount was apparent, evidencing the robust protection of surface P species, preventing phosphide from oxidizing on exposure to air. A shift of the 129 eV peak toward lower BE in the case of CoP_x/CoO-40 implies a high electron density in the P species, due to the modification of the electronic structure in the strongly coupled phase; this may enhance the electrochemical property.[32]

The high-resolution O 1s spectrum of CoP_x/CoO was deconvoluted into three peaks assigned to the Co–O bond (529.9 eV), O–P (531.3 eV), and surface-adsorbed water molecules (∼532.7 eV), as shown in **Figure 4c**. The surface composition of the CoO species was evaluated from the integral area of the peaks at 529.9 eV. The estimated surface CoO content in CP_x/CO-20 was ∼20 at%, which reduced to 11 at% for CP_x/CO-40, which also agrees with a decreasing trend in the CoO_{bulk} composition with increasing P (**Figure 2c**). A decrease in the surface CoO species with an increasing P source amount (CP_x/CO-20 and CP_x/CO-40) further corroborated

27

the controlled formation of CoO (surface/bulk) and CoP$_x$ components, which agrees with the Co 2p results on the reduced ratio of surface Co^{2+}(CoO)/Co^{3+}(CoP) species(**Figure 4d**). However, the surface CoO content was greater in CP$_x$/CO-100 (~14 at%), compared to that in CP$_x$/CO-40 (11 at%), despite the lower proportion of CoO$_{bulk}$ (6%) in the former (CoO$_{bulk}$=10% for CP$_x$/CO-40). This result further corroborated the formation of surface CoO isolates in CP$_x$/CO-100 as evidenced by the elemental mapping results (**Figure 2f**). Similarly, the higher proportion of Co^{2+} (CoO) in CP$_x$/CO-100 than that in CP$_x$/CO-40 was also evident from the Co^{2+}/Co^{3+} ratio derived using the Co 2p spectrum (**Figure 4d**). Besides, a shoulder at 534.1 eV in the O 1s XPS was observed for CP$_x$/CO-40, which is a feature that is obtained when the O/Co ratio is less than 1; in other words, the formation of the partial oxygen deficiency in CoO occurs at a slightly higher BE of 533.7 eV, as compared to that reported previously.[15] The partial oxygen deficiency in the CoO of CP$_x$/CO-40 may be related to the formation of metallic cobalt at the interface, as suggested by the Co 2p XPS (**Figure 4a**). Though the bulk CoO content (derived from XRD) increases when increasing the phosphorous source amount, the surface analysis shows an abrupt change in CoO composition at the surface (evaluated from Co 2p and O 1s XPS), as shown in **Figure 4d;** this reveals the alteration of the surface property of the CoP$_x$/CoO heterostructure. Although the bulk CoO content (~94%) is higher in CP$_x$/CO-100 than in CP$_x$/CO-40, the CoO isolates formed on the surface significantly reduced the electronic conductivity and eventually suppressed its supercapacitive performance. The aforenoted results demonstrate that both the bulk and surface compositions of the CoP$_x$/CoO heterostructure regulate the electronic and electrochemical properties altered by precise control of the phosphorous precursor. Therefore, the optimized CP$_x$/CO-40 with the composition of (CoP$_x$)$_{0.9}$/CoO$_{0.1}$ acquires a unique interfacial property from the interesting combination of

conducting metallic cobalt and a suitable CoP_x/CoO composition. This leads to enhanced charge-transport and electronic properties that are favorable for superior electrochemical performance.

Further, the usage of highly porous ZIFs as the initial precursor may significantly influence the electrochemical properties of the resultant CoP_x/CoO heterostructure. Hence, nitrogen sorption isotherm measurements were performed to evaluate the Brunauer–Emmett–Teller (BET) surface area, and the results are presented in **Figure 4e**. The BET surface area of the Co_3O_4-L is ~35.6 m^2 g^{-1}. After the phosphidation of Co_3O_4-L, the surface area of CP_x/CO-40 reduced to 22.0 m^2 g^{-1}, and this decreasing surface area was followed by a further increase in phosphorus content in CP_x/CO-100 (9.2 m^2 g^{-1}). This suppression of the surface area is a well-known phenomenon caused by the blockage or collapsing of pores during the phosphidation of the metal oxide precursor, which agrees with earlier reports.[39] In addition, the decreasing BET surface area agrees well with the Barrett–Joyner–Halenda (BJH) pore size distribution plot (**Figure S9, Supporting information**). Co_3O_4-L displays high porosity and contains copious macropores compared to the phosphorized samples. Despite having a high surface area, the Co_3O_4-L sample displayed a poor capacitance value of 35 F g^{-1} (**Figure S5, Supporting information**), while the phosphorized sample, CP_x/CO-40, exhibited an extremely high capacitance of 467 F g^{-1}, with a relatively low surface area (**Figure 4e**). This feature demonstrates the surface-area-independent electrochemical performance of phosphorized samples and is due to the high redox activity of phosphide and its intrinsic electronic conductivity.[40] Moreover, Raman spectroscopy was employed to characterize the CoO and CoP_x species and the nature of chemical bonding. The Raman spectra indicate the characteristic peaks of the Co-O (171, 450, 493, 589, and 654 cm^{-1}) and Co-P (minor 255 cm^{-1}) vibrational

modes (**Figure S10, Supporting information**). The graphene-like carbon peaks at ~1350 (D band) and 1550 cm^{-1} (G band) were absent for all the CoP$_x$/CoO samples; this suggests the presence of amorphous carbon, derived from the ZIF precursor, in the heterostructure.[41] Distinct Co-P and Co-O vibrations are apparent only in CP$_x$/CO-40 due to the appropriate CoP/CoO composition, while the negligible Co-P vibration in CP$_x$/CO-100 further suggests that the surface contains a high amount of CoO species, as evidenced from other results.

The high-performance CP$_x$/CO-40 heterostructure was further employed to form a reduced graphene oxide (RGO) composite (CP$_x$/CO-40-RGO) in the presence of 10 wt% GO, and its structural (surface/bulk) and electrochemical properties were evaluated. The PXRD of the pristine and graphene samples of CP$_x$/CO-40 was indexed with standard orthorhombic Co-P (CoP, Co$_2$P) and cubic CoO phases (**Figure S11** and **Table S3 Supporting information**), where CP$_x$/CO-40-RGO retained the same ratio of CoP$_x$ and CoO as that in CP$_x$/CO-40 with the bulk composition of (CoP$_x$)$_{0.9}$/CoO$_{0.1}$. The XPS were measured to further clarify the electronic structure and chemical composition of the CP$_x$/CO-40-RGO counterpart. Based on the Co 2p XPS results, (**Figure 5a)**, there was no apparent change in the oxidation state of Co, suggesting the presence of Co^{3+}, Co^{2+}, and partial metallic cobalt in the RGO composite. A substantial increase in the surface Co^{2+} (CoO) in CP$_x$/CO-40-RGO was apparent (Co^{2+}/Co^{3+} ratio = 1.5), compared to that in CP$_x$/CO-40 (Co^{2+}/Co^{3+} = ~1.0). Moreover, a strong PO$_x$ signal from CP$_x$/CO-40-RGO, due to surface oxidation of the metal phosphide on exposure to air, was apparent from the P 2p XPS (**Figure S12, Supporting information**). This result suggests that the presence of excess oxygen from the RGO functional groups may have enhanced the oxidation of surface phosphides. Besides, the O 1s XPS results exhibit a higher epoxide C–O content (~34 at%) for CP$_x$/CO-40-RGO, double the amount present in CP$_x$/CO-40 (~15 at%)

(**Figure 5b**). The higher epoxide C–O amount in CP$_x$/CO-40-RGO is derived from the oxygen bridges formed by the RGO sheets with the Co ions of the ZIF; moreover, this amount increases further during the air annealing of Co$_3$O$_4$-L/GO. Further Raman spectra were measured to evaluate the quality of the RGO sheets in the composite sample. Although the typical D- and G-carbon bands were observed in the GO and ZIF-Co-L/GO precursor, the graphene bands disappeared in the Co$_3$O$_4$-L/GO, CP$_x$/CO-40, and CP$_x$/CO-40-RGO samples. This suggests that the surface oxidation of GO leads to higher oxygen functionalization during the air annealing step (400 °C) of the Co$_3$O$_4$-L/GO synthesis (**Figure 5c**). Besides, the oxygen-functionalized GO sheets were expected to exhibit partially reduced oxygen bridges owing to the PH$_3$ gas during phosphidation. Notably, the decomposition of GO may be ruled out at the low temperature of 400 °C (Co$_3$O$_4$-L synthesis), as it degrades at a higher temperature of $\geq$600 °C under air.[42] Both the Co-O and Co-P vibrational modes were apparent in the phosphorized CoP$_x$/CoO sample, whereas only the Co-O vibrational modes were noted in the ZIF-Co-L/GO and Co$_3$O$_4$-L/GO samples. The energy dispersive x-ray analysis (EDAX) from SEM results reveal that the oxygen content in CP$_x$/CO-40-RGO (~27 at%) is approximately twice higher than that in CP$_x$/CO-40 (~15 at%), further reaffirming the surface oxidation of RGO during air annealing, leading to excess oxygen species in the RGO sheets (inset **Figure 5d**). The leaf-like morphology of the CP$_x$/CO-40 (**Figure 5e**) was retained in the CP$_x$/CO-40-RGO (**Figure 5f**), with uniformly distributed leaf-shapes over the RGO sheets.

31
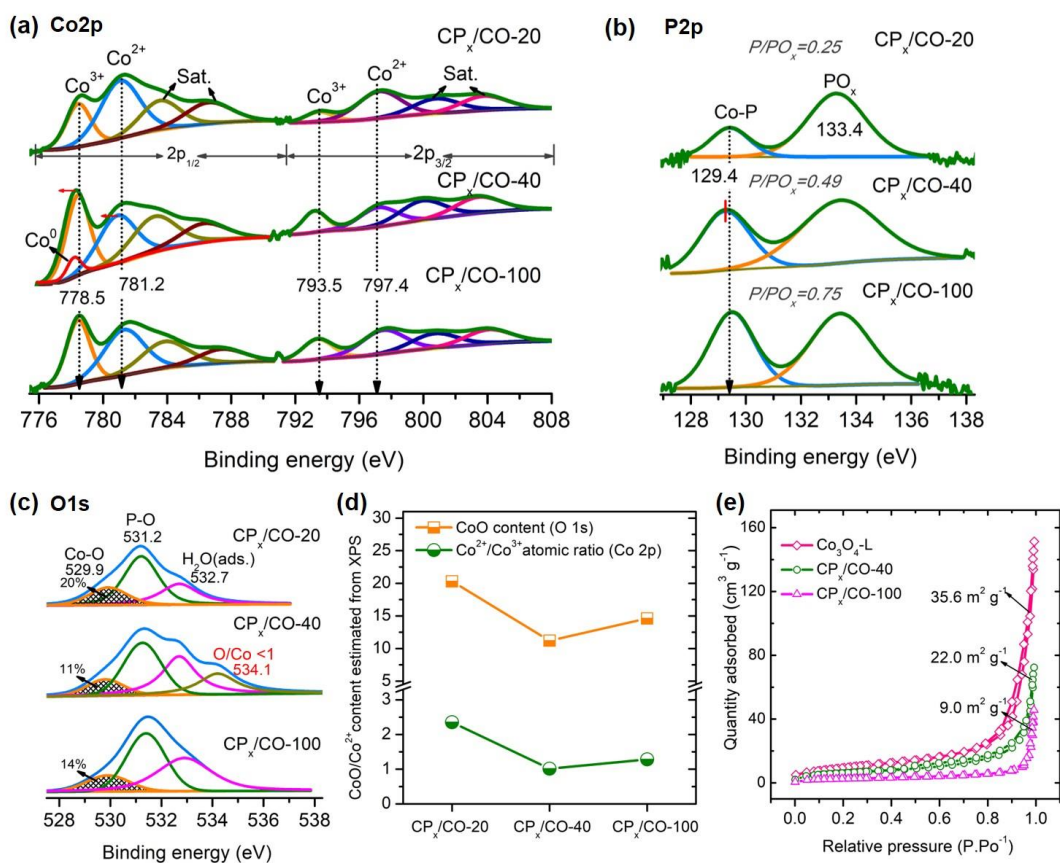
Figure 4. Surface states of CoP$_x$/CoO heterostructure with varying P content. XPS spectra of (a) Co 2p, (b) P 2p, and (c) O 1s of CoP$_x$/CoO; (d) relationship between phosphorous precursor and quantified surface CoO species (O 1s XPS) and atomic ratio of Co^{2+}/Co^{3+} of the CoP$_x$/CoO derived from Co 2p XPS, (e) BET surface nitrogen adsorption/desorption isotherms of Co$_3$O$_4$-L, CoP$_x$/CoO-40, and CoP$_x$/CoO-100 and their corresponding surface area.

Furthermore, the electrochemical behaviors of the CP$_x$/CO-40 and CP$_x$/CO-40/RGO analogs were investigated using a three-electrode setup. The comparison of their CV curves reveals redox peaks in both the samples, suggesting the faradaic behavior of the electrodes, as shown in **Figure 5g**. The enclosed CV area of the CP$_x$/CO-40-RGO is lower than that of the CP$_x$/CO-40 in the same potential range (**Figure 5g**). Similarly, the specific capacitance was estimated from the GCD profiles (**Figure S13** and **S14**, **Supporting information**) as a function of varying current densities (5–30 A g^{-1}); CP$_x$/CO-40-RGO exhibited lower capacitance values at most of

the current densities (**Figure 5h**), i.e., the specific capacitance of CP$_x$/CO-40-RGO (438 F g^{-1}) was slightly lower than that of the CP$_x$/CO-40 (466 F g^{-1}) at 5 A g^{-1}. This trend illustrates the presence of the oxygen-rich GO evidenced from the XPS and SEM EDAX results and may significantly reduce the electronic property of the CP$_x$/CO-40-RGO sample. Furthermore, the reduced electronic property of the CP$_x$/CO-40-RGO was confirmed from the EIS, depicting its higher charge-transfer resistance than that of the CP$_x$/CO-40 electrode (**Figure 5i**). The excellent electrical conductivity of the CP$_x$/CO-40 is conducive to the charge-storage capability and the interfacial property due to the reduced charge-transfer resistance. The interfacial property of the CP$_x$/CO-40 sample was absent in the RGO analog due to the insulating oxygen-rich RGO surface formed during the synthesis of the Co$_3$O$_4$-L intermediate in the air. The cycling stability was tested using GCD cycles at a high current density of 30 A g^{-1} to demonstrate the cycling performance of the CP$_x$/CO-40-RGO analog. Despite a lower capacitance, the CP$_x$/CO-40-RGO achieved high cycling stability with capacitance retention of 107% after 10000 cycles calculated by considering capacitance at the 600th cycle as the initial capacitance to avoid the activation process (**Figure 5j**). While the pristine CP$_x$/CO-40 exhibited a capacitance retention of ~91%. The superior cycling stability of the CP$_x$/CO-40-RGO is attributed to the effective encapsulation of CoP$_x$/CoO that prevents particle pulverization during cycling while ensuring effective particle-particle contact. Further, postmortem SEM analysis of the electrodes after 10000 cycles was conducted to analyze the stability of the electrode. The cycled electrodes retained the leaf-like morphology, with surface roughness owing to the hydroxide formation, affirming the robustness of the heterostructure (**Figure 5k, l**). Higher roughness was apparent for CP$_x$/CO-40 (**Figure 5k**) than for CP$_x$/CO-40-RGO (**Figure 5l**), further corroborating the higher cycling stability of the latter. Furthermore, a negligible

33

phosphorous content (<3 at%) was noted after 10000 cycles, as seen from the EDAX results (**Figure 5m**). This small content denotes the conversion of cobalt phosphide to its hydroxides (**Table S4, Supporting information**). Hence, the inferior capacitive performance of the CP_x/CO-40-RGO compared to the CP_x/CO-40 can be ascribed to the rich oxygen functionalization on the RGO surface that considerably increased the resistance, eventually reducing the charge-storage property. The excellent cycling stability of both analogs (>90%) is attributed to the robust morphology of the leaf-like CoP_x/CoO heterostructure with well-interconnected CoP_x and CoO and the metallic cobalt formed at the interfaces.
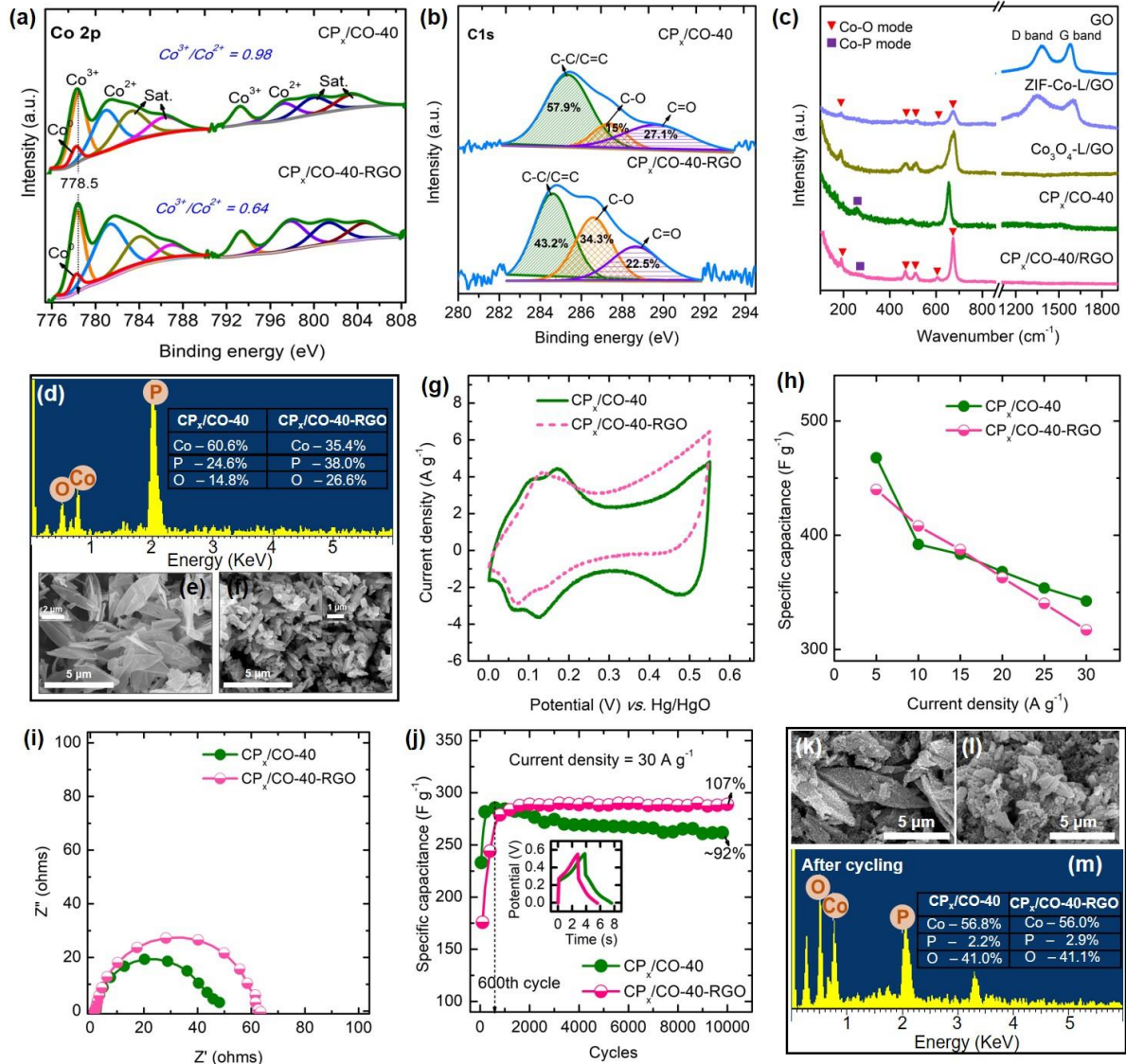
Figure 5. Structural and electrochemical evaluation of graphene-based CoP$_x$/CoO-40-RGO heterostructure. XPS of (a) Co 2p and (b) P 2p of CP$_x$/CO-40 and CP$_x$/CO-40-RGO; (c) Raman spectra; (d) SEM EDAX of CP$_x$/CO-40 (inset depicting the atomic% of Co, P, and O elements); SEM of (e) CP$_x$/CO-40 and (f) CP$_x$/CO-40-RGO; (g) CV at a scan rate of 5 mV s^{-1}; (h) specific capacitance at different current densities; (i) EIS spectra; and (j) cycling stability measured at a current density of 30 A g^{-1} (capacitance retention was calculated between the 600th and 10000th cycles); inset depicts GCD profile at the 1st cycle; postmortem SEM images of electrodes after 10000 cycles of (k) CP$_x$/CO-40 and (l) CP$_x$/CO-40-RGO; (m) SEM EDAX of CP$_x$/CO-40 electrodes after 10000 cycles (inset depicting atomic% of Co, P, and O elements).

35

The practical application of the developed electroactive materials for energy storage was assessed by fabricating an asymmetric supercapacitor prototype device using the CoP_x/CoO-40 heterostructure and the NPC@rGO (N-doped porous carbon@graphene sheets) as the positive and negative electrodes, respectively. The total loading mass of the active materials for the asymmetric supercapacitor was ~4.3 mg. The electrochemical properties of the NPC@rGO negative electrode were evaluated based on their CV and GCD curves in a three-electrode system using 2 M KOH electrolyte (**Figure S15, Supporting information**). The specific capacitance of the NPC@rGO negative electrode was calculated from the GCD curves and was found to be ~155 F g^{-1} at 5 A g^{-1} (**Figure S15c, Supporting information**), which is a reasonable value compared with those of reported carbon-based negative electrodes [35, 36]. The high specific capacitance of ~364 F g^{-1} obtained at 5 A g^{-1} for the CP_x/CO-40 electrode suggests that the major contribution to the capacitance of the ASC device originates from the developed CoP_x/CoO heterostructure electrode. Before fabricating the two-electrode assembly, the mass loading of the two electrode materials was balanced according to GCD curves at 5 A g^{-1} to obtain high capacitance for the device and ensure the charge balance between the electrodes. Comparative CV curves of both the positive and negative electrodes were measured at a scan rate of 5 mV s^{-1} (**Figure 6a**). The CP_x/CO-40 positive electrode operated at the potential window of 0–0.6 V, exhibiting battery-type faradaic behavior, whereas the NPC@rGO negative electrode operated at the potential range between -1.0 and 0 V, exhibiting an electric double-layer structure with a rectangular curve. Thus, the asymmetric supercapacitor device could function at a stable electrochemical potential of up to 1.6 V. The CV curves of the asymmetric supercapacitor (ASC) device were measured at different scan rates at the potential window of 1.6 V; the ASC device exhibited integrated features of electric double-layer and

battery-type faradaic behavior of the negative NPC@rGO and positive CoP$_x$/CoO electrodes (**Figure 6b**).

The GCD curves of the ASC device exhibited symmetric charge/discharge curves with a negligible voltage drop, which further reflects the ideal capacitive behavior, good reversibility, and a fast charge-discharge process (**Figure 6c**). The calculated specific capacitances at various current densities of 0.5, 1, 2, 3, 4, 5, and 6 A g^{-1} were ~38, 36, 35, 34, ~33, ~32, and ~31 F g^{-1}, respectively (**Figure 6d**), with capacitance retention of ~84% at 5 A g^{-1}, indicating the excellent rate capability of the CP$_x$/CO-40‖NPC@rGO device. The Ragone plot of the ASC device was developed from GCD curves at variable current densities; thus, energy density and power density were elucidated and are shown in **Figure 6e**. The CP$_x$/CO-40‖NPC@rGO supercapacitor realized a reasonable energy density of 12.7 Wh kg^{-1} at ~0.39 kW kg^{-1} and could deliver up to 10.4 Wh kg^{-1} at 4.6 kW kg^{-1}. The energy density of the device is comparable and even higher than many oxide and phosphide-based hybrid supercapacitors, namely NiCo$_2$O$_4$‖AC (6.8 Wh kg^{-1} at 2.8 kW kg^{-1}) [43], Graphene‖Co$_2$P (8.8 Wh kg^{-1} at 6.0 kW kg^{-1}) [35], NiCo$_2$S$_4$‖PC(10.6 Wh kg^{-1} at 2.5 kW kg^{-1}) [44], and Co$_3$P$_2$O$_8$‖AC (11.9 Wh kg^{-1} at 3.6 kW kg^{-1}) [45]. The superior energy density of the ASC device is attributable to the high specific capacitance of the CoP$_x$/CoO heterostructure electrode at a wide potential window of 0–1.6 V in an aqueous electrolyte. Furthermore, higher energy/power density values could be achieved by employing better performing carbonaceous negative electrodes with a deliverable capacitance exceeding 160 F g^{-1}, as reported in the literature [35, 36]. The electrochemical impedance spectral analysis would provide insights into the electrical conductivity of materials at bulk and at the electrode/electrolyte interface; A Nyquist plot of the device is presented in **Figure 6f.** The low evaluated charge transfer resistance (Rct) of 0.8 Ω (inset of **Figure 6f**) favored the superior

37

energy density of the ASC device. The low Rct is derived primarily from the heterostructure positive electrode (high conductive CoP, metallic Co, and CoP$_x$/CoO interface) and the NPC@rGO, which may favor the fast electron transfer in the device and, eventually, a higher energy density. A vertical line in the low-frequency region indicated the capacitive behavior of the ASC device.

Further, the cycling stability of the CP$_x$/CO-40||NPC@rGO device was evaluated for practical supercapacitor applications by performing charge/discharge cycles at a current density of 3 A g^{-1}; the results are presented in **Figure 6g**. An initial specific capacitance of ~25 F g^{-1} was obtained at 3 A g^{-1}, which rapidly increased to a maximum capacitance of ~34 F g^{-1} at 600 cycles owing to the activation caused by the slow wettability of carbon cloth. Therefore, the calculated capacitance retention between the 600th and 10000th cycles is ~93%, indicating the superior long-term stability of the ASC device [35]. The superior electrochemical performance of the CoP$_x$/CoO-40 heterostructure electrode can be attributed to 1) the tight contact between the well-integrated CoP$_x$ and CoO components in the leaf-like micron-sized heterostructure that prevents a high heterojunction resistance while improving the faradaic reaction and cycling stability; 2) the controlled conductive CoP$_x$ and CoO components and their synergistic effect promote a facile ion/charge transport in the electrodes that ensure rich redox reactions, thereby enhancing the electrochemical properties; and 3) the critical role of the interfacial property in the CoP$_x$-rich optimized CoP$_x$/CoO heterostructure in imparting enhanced electronic conductivity from metallic cobalt and higher charge storage properties. Hence, the composition-engineered CoP$_x$-rich CoP$_x$/CoO heterostructure could be a suitable alternative electrode for supercapacitor applications.
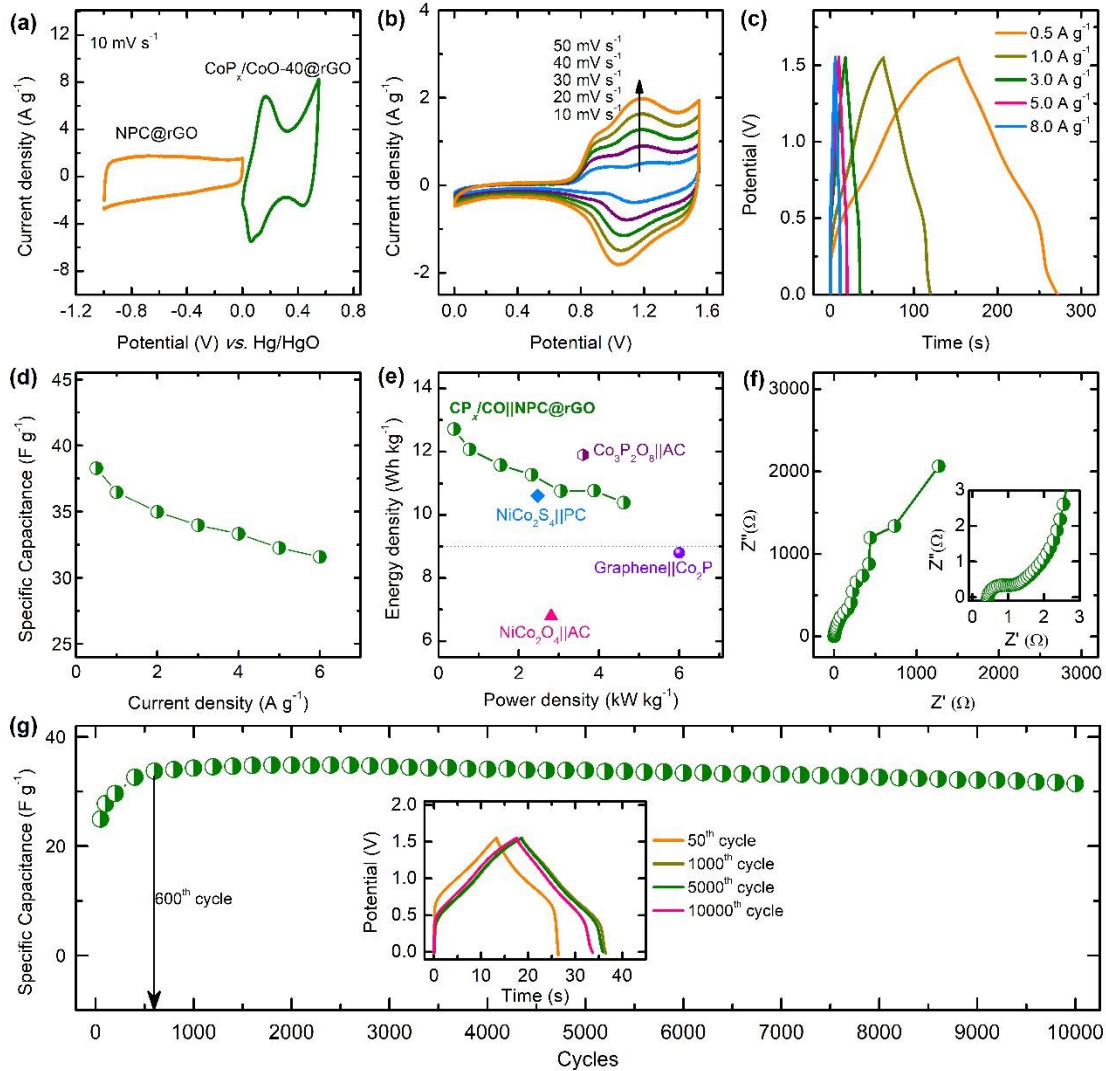
Figure 6. Asymmetric supercapacitor device (CP$_x$/CO-40||NPC@rGO). (a) CV curves of CoP$_x$/CoO-40 and NPC@rGO (N-doped porous carbon@graphene sheets), used as the positive and negative electrodes, respectively; (b) CV curves of the device at variable scan rates in the potential range of 0–1.6 V; (c) GCD profiles at variable current densities and (d) specific capacitances at variable current densities; (e) Ragone plot of the fabricate device indicating their energy and power densities, and compared with the previous reported two-electrode supercapacitor namely NiCo$_2$O$_4$||AC [43], graphene||Co$_2$P [35], NiCo$_2$S$_4$||PC [44], Co$_3$P$_2$O$_8$||AC [45]; (f) Nyquist plot of the asymmetric device (inset: high-frequency region) and (g) cycling stability at a current density of 3 A g^{-1} as a function of 10000 cycles (inset: GCD profiles of selected cycles).

4. Conclusions

A novel CoP_x/CoO heterostructure was synthesized successfully from a leaf-like 2D ZIF-Co-L molecular precursor, and its electrochemical performance was evaluated. The CoP_x/CoO heterostructure combined the properties of high redox-active and conducting cobalt phosphide and high structural stability of cobalt monoxide, which showed enhanced supercapacitive properties. Compositional variation in the $(CoP_x)_{1-y}/CoO_y$ heterostructure ($0.44 > y > 0.06$) altered the electronic structure and, eventually, the electrochemical performance of supercapacitor device, influenced by the phase fractions of the CoP and CoO components. The $(CoP_x)_{0.9}/(CoO)_{0.1}$ composition displayed high specific capacitance (466 F g^{-1}) and long-term cycle stability (91% over 10000 cycles) owing to their efficient lateral coupling of components, optimized composition, synergistic effect, and unique interfaces that form metallic cobalt. The $(CoP_x)_{0.9}/(CoO)_{0.1}$-based asymmetric device exhibited a higher energy density of 12.7 Wh kg^{-1} at a power density of 370 W kg^{-1} than the reported oxide-phosphide-based devices and demonstrated better cycle stability (~93%) even after 10000 cycles. Therefore, designing compositionally varied oxide/phosphide-based heterostructure electrodes would be an attractive and beneficial approach for the development of high-performance energy storage devices.

40

Supporting information

Supporting information is available from the Science direct library or the author.

References

[1] D.G. Mackanic, T.-H. Chang, Z. Huang, Y. Cui, Z. Bao, Stretchable electrochemical energy storage devices, Chem. Soc. Rev., 49 (2020) 4466-4495.

[2] S. Zou, X. Liu, Z. Xiao, P. Xie, K. Liu, C. Lv, Y. Yin, Y. Li, Z. Wu, Engineering the interface for promoting ionic/electronic transmission of organic flexible supercapacitors with high volumetric energy density, J. Power Sources, 460 (2020) 228097.

[3] C. Arbizzani, Y. Yu, J. Li, J. Xiao, Y.-y. Xia, Y. Yang, C. Santato, R. Raccichini, S. Passerini, Good practice guide for papers on supercapacitors and related hybrid capacitors for the Journal of Power Sources, J. Power Sources, 450 (2020) 227636.

[4] Chandu V.V. Muralee Gopi, P.J. Singh Rana, R. Padma, R. Vinodh, H.-J. Kim, Selective integration of hierarchical nanostructured energy materials: an effective approach to boost the energy storage performance of flexible hybrid supercapacitors, J. Mater. Chem. A, 7 (2019) 6374-6386.

[5] T. Ruan, B. Wang, Y. Yang, X. Zhang, R. Song, Y. Ning, Z. Wang, H. Yu, Y. Zhou, D. Wang, H. Liu, S. Dou, Interfacial and Electronic Modulation via Localized Sulfurization for Boosting Lithium Storage Kinetics, Adv. Mater., 32 (2020) 2000151.

[6] S.V.P. Vattikuti, Chapter 4 - Heterostructured Nanomaterials: Latest Trends in Formation of Inorganic Heterostructures, in: S. Mohan Bhagyaraj, O.S. Oluwafemi, N. Kalarikkal, S. Thomas (Eds.) Synthesis of Inorganic Nanomaterials, Woodhead Publishing, 2018, pp. 89-120.

[7] Y. Lin, K. Sun, S. Liu, X. Chen, Y. Cheng, W.-C. Cheong, Z. Chen, L. Zheng, J. Zhang, X. Li, Y. Pan, C. Chen, Construction of CoP/NiCoP Nanotadpoles Heterojunction Interface for Wide pH Hydrogen Evolution Electrocatalysis and Supercapacitor, Adv. Energy Mater., 9 (2019) 1901213.

[8] Y. Wang, Y. He, M. Zhou, Fabrication of hierarchical $Co(OH)_2$@$Ni(OH)_2$ core-shell nanosheets on carbon cloth as an advanced electrocatalyst for oxygen evolution reaction, Appl. Surf. Sci., 479 (2019) 1270-1276.

[9] H. Liang, C. Xia, Q. Jiang, A.N. Gandi, U. Schwingenschlögl, H.N. Alshareef, Low temperature synthesis of ternary metal phosphides using plasma for asymmetric supercapacitors, Nano Energy, 35 (2017) 331-340.

[10] L. Wan, C. He, D. Chen, J. Liu, Y. Zhang, C. Du, M. Xie, J. Chen, In situ grown $NiFeP$@$NiCo_2S_4$ nanosheet arrays on carbon cloth for asymmetric supercapacitors, Chem. Eng. J., 399 (2020) 125778.

[11] C. Zhou, Y. Zhang, Y. Li, J. Liu, Construction of High-Capacitance 3D CoO@Polypyrrole Nanowire Array Electrode for Aqueous Asymmetric Supercapacitor, Nano Lett., 13 (2013) 2078-2085.

[12] J. Wang, R. Gao, L. Zheng, Z. Chen, Z. Wu, L. Sun, Z. Hu, X. Liu, CoO/CoP Heterostructured Nanosheets with an O–P Interpenetrated Interface as a Bifunctional Electrocatalyst for Na–O$_2$ Battery, ACS Catal., 8 (2018) 8953-8960.

[13] Z. Liu, G. Zhang, K. Zhang, H. Lan, H. Liu, J. Qu, Low electronegativity Mn bulk doping intensifies charge storage of Ni_2P redox shuttle for membrane-free water electrolysis, J. Mater. Chem. A, 8 (2020) 4073-4082.

[14] Y. Hu, M. Liu, Q. Yang, L. Kong, L. Kang, Facile synthesis of high electrical conductive CoP via solid-state synthetic routes for supercapacitors, J. Energy Chem., 26 (2017) 49-55.

[15] X. Hu, S. Zhang, J. Sun, L. Yu, X. Qian, R. Hu, Y. Wang, H. Zhao, J. Zhu, 2D Fe-containing cobalt phosphide/cobalt oxide lateral heterostructure with enhanced activity for oxygen evolution reaction, Nano Energy, 56 (2019) 109-117.

42

[16] T. Su, Q. Shao, Z. Qin, Z. Guo, Z. Wu, Role of Interfaces in Two-Dimensional Photocatalyst for Water Splitting, ACS Catal., 8 (2018) 2253-2276.

[17] B. Chen, Z. Yang, Y. Zhu, Y. Xia, Zeolitic imidazolate framework materials: recent progress in synthesis and applications, J. Mater. Chem. A, 2 (2014) 16811-16831.

[18] C.-H. Kuo, Y. Tang, L.-Y. Chou, B.T. Sneed, C.N. Brodsky, Z. Zhao, C.-K. Tsung, Yolk–Shell Nanocrystal@ZIF-8 Nanostructures for Gas-Phase Heterogeneous Catalysis with Selectivity Control, J. Am. Chem. Soc., 134 (2012) 14345-14348.

[19] S. Gayathri, P. Arunkumar, J.H. Han, Scanty graphene-driven phase control and heteroatom functionalization of ZIF-67-derived CoP-draped N-doped carbon/graphene as a hybrid electrode for high-performance asymmetric supercapacitor, J. Colloid Interface Sci., 582 (2021) 1136-1148.

[20] Z. Chen, Y. Ha, H. Jia, X. Yan, M. Chen, M. Liu, R. Wu, Oriented Transformation of Co-LDH into 2D/3D ZIF-67 to Achieve Co–N–C Hybrids for Efficient Overall Water Splitting, Adv. Energy Mater., 9 (2019) 1803918.

[21] W. Wang, L. Zhang, G. Xu, H. Song, L. Yang, C. Zhang, J. Xu, D. Jia, Structure-designed synthesis of CoP microcubes from metal–organic frameworks with enhanced supercapacitor properties, Inorg. Chem., 57 (2018) 10287-10294.

[22] K. Subramani, N. Sudhan, R. Divya, M. Sathish, All-solid-state asymmetric supercapacitors based on cobalt hexacyanoferrate-derived CoS and activated carbon, RSC Adv., 7 (2017) 6648-6659.

[23] H. Rietveld, A profile refinement method for nuclear and magnetic structures, J. Appl. Crystallogr., 2 (1969) 65-71.

[24] J. Rodríguez-Carvajal, Recent advances in magnetic structure determination by neutron powder diffraction, Phys. B, 192 (1993) 55-69.

[25] S. Rundqvist, P.C. Nawapong, G. Widmark, P. Nielsen, B. Sjöberg, E. Larsen, Crystal Structure Refinements of some MnP-type Phosphides, Acta Chem. Scand, 19 (1965).

[26] R. Skála, M. Drábek, The crystal structure of Co_2P from X-ray powder diffraction data and its mineralogical applications, Bull. Czech Geol. Surv, 76 (2001) 209-216.

[27] N. Tombs, H. Rooksby, Structure of monoxides of some transition elements at low temperatures, Nature, 165 (1950) 442-443.

[28] J. Zhang, T. Zhang, D. Yu, K. Xiao, Y. Hong, Transition from ZIF-L-Co to ZIF-67: a new insight into the structural evolution of zeolitic imidazolate frameworks (ZIFs) in aqueous systems, CrystEngComm, 17 (2015) 8212-8215.

[29] X. Wang, H. Xue, Z. Na, D. Yin, Q. Li, C. Wang, L. Wang, G. Huang, Metal organic frameworks route to prepare two-dimensional porous zinc-cobalt oxide plates as anode materials for lithium-ion batteries, J. Power Sources, 396 (2018) 659-666.

[30] R. Chen, J. Yao, Q. Gu, S. Smeets, C. Baerlocher, H. Gu, D. Zhu, W. Morris, O.M. Yaghi, H. Wang, A two-dimensional zeolitic imidazolate framework with a cushion-shaped cavity for CO_2 adsorption, Chem. Commun., 49 (2013) 9500-9502.

[31] D. Liu, X. Li, L. Wei, T. Zhang, A. Wang, C. Liu, R. Prins, Disproportionation of hypophosphite and phosphite, Dalton trans., 46 (2017) 6366-6378.

[32] Y. Niu, M. Xiao, J. Zhu, T. Zeng, J. Li, W. Zhang, D. Su, A. Yu, Z. Chen, Trimurti Heterostructured Hybrid with Intimate CoO/Co_xP Interface as Robust Bifunctional Air Electrode for Rechargeable Zn-air Batteries, J. Mater. Chem. A, (2020).

[33] H.J. Fan, U. Gösele, M. Zacharias, Formation of nanotubes and hollow nanoparticles based on Kirkendall and diffusion processes: a review, small, 3 (2007) 1660-1671.

43

[34] T. Wang, L. Wu, X. Xu, Y. Sun, Y. Wang, W. Zhong, Y. Du, An efficient Co_3S_4/CoP hybrid catalyst for electrocatalytic hydrogen evolution, Sci. Rep., 7 (2017) 11891.

[35] X. Chen, M. Cheng, D. Chen, R. Wang, Shape-Controlled Synthesis of Co_2P Nanostructures and Their Application in Supercapacitors, ACS Appl. Mater. Interfaces, 8 (2016) 3892-3900.

[36] M. Cheng, H. Fan, Y. Xu, R. Wang, X. Zhang, Hollow Co_2P nanoflowers assembled from nanorods for ultralong cycle-life supercapacitors, Nanoscale, 9 (2017) 14162-14171.

[37] N. Tang, W. Wang, H. You, Z. Zhai, J. Hilario, L. Zeng, L. Zhang, Morphology tuning of porous CoO nanowall towards enhanced electrochemical performance as supercapacitors electrodes, Catal. Today, 330 (2019) 240-245.

[38] W. Zhu, W. Zhang, Y. Li, Z. Yue, M. Ren, Y. Zhang, N.M. Saleh, J. Wang, Energy-efficient 1.67 V single-and 0.90 V dual-electrolyte based overall water-electrolysis devices enabled by a ZIF-L derived acid–base bifunctional cobalt phosphide nanoarray, J. Mater. Chem. A, 6 (2018) 24277-24284.

[39] S. Gayathri, P. Arunkumar, E.J. Kim, S. Kim, I. Kang, J.H. Han, Mesoporous nitrogen-doped carbon@graphene nanosheets as ultra-stable anode for lithium-ion batteries − Melamine as surface modifier than nitrogen source, Electrochim. Acta, 318 (2019) 290-301.

[40] Y. Lan, H. Zhao, Y. Zong, X. Li, Y. Sun, J. Feng, Y. Wang, X. Zheng, Y. Du, Phosphorization boosts the capacitance of mixed metal nanosheet arrays for high performance supercapacitor electrodes, Nanoscale, 10 (2018) 11775-11781.

[41] S.-K. Jerng, D. Seong Yu, J. Hong Lee, C. Kim, S. Yoon, S.-H. Chun, Graphitic carbon growth on crystalline and amorphous oxide substrates using molecular beam epitaxy, Nanoscale Research Letters, 6 (2011) 565.

[42] X. Chen, D. Meng, B. Wang, B.-W. Li, W. Li, C.W. Bielawski, R.S. Ruoff, Rapid thermal decomposition of confined graphene oxide films in air, Carbon, 101 (2016) 71-76.

[43] R. Ding, L. Qi, M. Jia, H. Wang, Facile and large-scale chemical synthesis of highly porous secondary submicron/micron-sized $NiCo_2O_4$ materials for high-performance aqueous hybrid $AC-NiCo_2O_4$ electrochemical capacitors, Electrochim. Acta, 107 (2013) 494-502.

[44] W. Kong, C. Lu, W. Zhang, J. Pu, Z. Wang, Homogeneous core–shell $NiCo_2S_4$ nanostructures supported on nickel foam for supercapacitors, J. Mater. Chem. A, 3 (2015) 12452-12460.

[45] J.-J. Li, M.-C. Liu, L.-B. Kong, M. Shi, W. Han, L. Kang, Facile synthesis of $Co_3P_2O_8 \cdot 8H_2O$ for high-performance electrochemical energy storage, Mater. Lett., 161 (2015) 404-407.

Graphical abstract
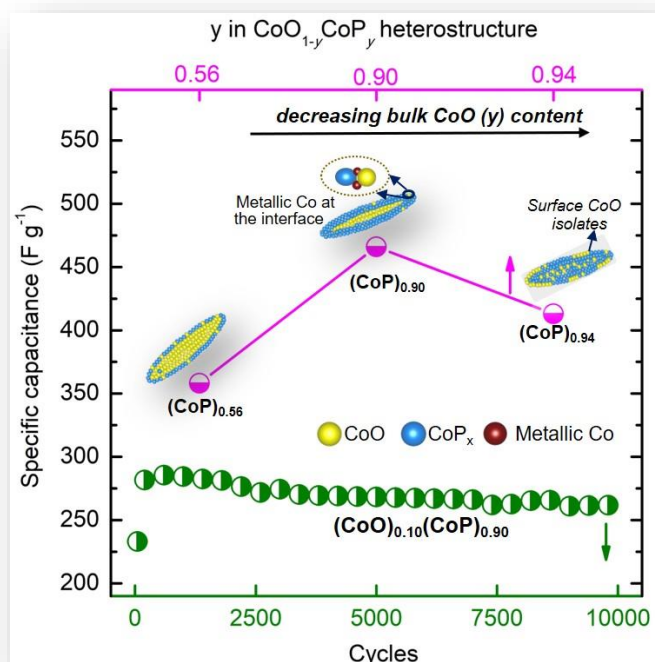
Highlights

- Leaf-like CoP_x/CoO heterostructure was synthesized from a ZIF-Co-L precursor.

- Synergy of CoP_x and CoO guarantees the interfacial property and enhances energy storage.

- Controlled phosphidation regulated the bulk/surface composition of CoP_x/CoO.

- $(CoP_x)_{0.9}$/$CoO_{0.1}$ showed high capacitance derived from interface-driven metallic Co.

- Asymmetric supercapacitor displays high energy density of 12.7 Wh kg^{-1} at 370 W kg^{-1}.